CONTROL AND PERCEPTION FOR AUTONOMOUS DRIVING

A Dissertation

by

VAMSI KRISHNA VEGAMOOR

Submitted to the Office of Graduate and Professional Studies of
Texas A&M University
in partial fulfillment of the requirements for the degree of

DOCTOR OF PHILOSOPHY

Co-Chairs of Committee,	Swaroop Darbha
	Sivakumar Rathinam
Committee Members,	Prabhakar Pagilla
	Dezhen Song
Head of Department,	Guillermo Aguilar

December 2021

Major Subject: Mechanical Engineering

ABSTRACT

Autonomous driving requires perception and control. The first part of the dissertation is focused on an aspect of control related to automatic vehicle following that is not well understood, namely, the influence of imperfect wireless connectivity in vehicle platooning applications. The primary goal of most research in vehicle platooning is to enable the shortest inter vehicular spacing while maintaining safety, since short following distances are known to improve fuel efficiency and traffic mobility. It is also known that wireless connectivity can be exploited to achieve tighter platoon formations, but the effect of imperfections of wireless links on platoon stability were not well understood. This work proposes an algorithm to estimate the smallest time headway that guarantees safety based on the average packet reception rate. The algorithm has been corroborated using Model in Loop (MIL) simulations as well as test runs with a hybrid car. This thesis also develops a method to estimate the maximum perturbation in spacing error of any vehicle in a string stable platoon based on the lead vehicle's acceleration maneuver. This allows a designer to pick a safe standstill distance.

The second part of this dissertation explores the challenges of environment perception and sensor fusion under adverse visibility conditions for autonomous driving. The sensor stack for autonomous vehicles usually consists of on one or more of radars, visible spectrum/RGB (Red-Green-Blue) cameras and lidars. RGB cameras perform poorly in low light conditions (at night) as well as in direct sunlight. While automotive radars are resilient to environmental conditions, they only offer a low resolution output. In this thesis, we explore the benefits of combining a Long Wavelength Infrared (LWIR) thermal camera with a radar sensor for detection and tracking of vehicles/pedestrians in poor visibility conditions. A modified Joint Probabilistic Data Association (JPDA) filter is implemented on real-world data to demonstrate the feasibility of the proposed system.

ACKNOWLEDGMENTS

First, I would like to express gratitude to my parents for their continuous support through all my endeavors.

I am deeply indebted to my committee chair, Dr. Swaroop Darbha and co-chair Dr. Sivakumar Rathinam for taking me under their wings when I transferred to the mechanical engineering department in early 2017. I have since benefited from their guidance on how to be a competent researcher and am thankful for their mentorship over the past five years. I am also grateful to my thesis committee members Dr. Prabhakar Pagilla and Dr. Dezhen Song for their feedback on this work.

I would like to acknowledge the graduate students in the Systems, Control and Optimization, Autonomous Systems, Unmanned Systems and the Connected, Autonomous Safe Technologies (CAST) research groups for many interesting discussions and personal friendships. Special thanks to Abhay Bhadoriya for helping me with numerous data collection sessions.

On a lighter note, I am also thankful to the ancient discoverers of coffee as the beverage has helped me cram through deadlines and stay productive.

CONTRIBUTORS AND FUNDING SOURCES

Contributors

This work was supported by a dissertation committee consisting of Professors Swaroop Darbha (chair), Sivakumar Rathinam (co-chair) and Prabhakar Pagilla of the Department of Mechanical Engineering, and Professor Dezhen Song of the Department of Computer Science.

All other work conducted for the dissertation was completed by the student independently.

Funding Sources

This work received financial support from Safety Through Disruption (SAFE-D) project 04-117, the US Department of Transportation through the Dwight D. Eisenhower Fellowships (Grant numbers: 693JJ32145049 and 693JJ32045024) as well as the J. George Thompson graduate fellowship from the mechanical engineering department at Texas A&M University.

NOMENCLATURE

AVFS	Automatic Vehicle Following Systems
ACC	Adaptive Cruise Control
CACC	Cooperative Adaptive Cruise Control (one-vehicle lookup)
CACC+	Cooperative Adaptive Cruise Control (two-vehicle lookup)
DSRC	Direct Short Range Communication
JPDA	Joint Probabilistic Data Association
RGB	Red-Green-Blue; refers to cameras that work with the visible spectrum
h_w	Time headway used in the control policy for vehicle platooning. Usually expressed in seconds.
τ	Parasitic/actuation lag in the vehicle.
x_i, v_i, a_i	Position, velocity and acceleration of the i^{th} vehicle.
e_i	Spacing error of the i^{th} vehicle with reference to the vehicle in front.

TABLE OF CONTENTS

Page

LIST OF FIGURES

FIGURE Page

LIST OF TABLES

TABLE Page

1. INTRODUCTION

The last two decades have seen a renewed interest in autonomous vehicles, arguably spurred on by the DARPA Grand challenges in the mid 2000s.While the DARPA Grand challenges were primarily aimed at showcasing the feasibility of autonomous driving, there is a potential to use them in improving traffic safety. We know that over 30,000 people are involved in fatal crashes in the United States alone, the majority of which are caused by human negligence or error [1, 2]. Naturally, the goal of self-driving technology is to prevent *avoidable* crashes by removing the human out of the system while improving traffic flow and fuel efficiency. Although this thesis recognizes that human intuition plays a significant role in the safety and that it needs to be better quantified and understood, this thesis focuses on developing technology that makes self-driving feasible.

With the addition of wireless communication capabilities, Connected and Autonomous Vehicles (CAVs) have the potential to improve mobility on roadways by utilizing information from neighboring vehicles as well as information from 'smart' infrastructure. Consequently, the first part of this work (chapters 2 to 5) covers Automatic Vehicle Following Systems (AVFS) with a focus on safety guarantees for vehicle platoons.

The Society of automotive Engineers has classified self-driving vehicle capabilities into different levels [3]. A key requirement of the highest level of automation ('Level 5') is that such a vehicle must be able to perform all driving functions *under all conditions*, without the need for any human intervention. A big part of the challenge in achieving Level 5 autonomy is maintaining functionality outside of nominal operating conditions (edge cases). The second part of this thesis (chapters 6 to 8) focuses on the perception system of autonomous vehicles and explore solutions to tackle adverse visibility conditions.

A brief background and the main contributions of each of these two parts are provided below.

1.1 Automatic Vehicle Following Systems

It is humbling to note that vehicle platooning has been studied since the late 1950s, predating many of the computing and sensing technologies that are taken for granted today. Figure 1.1 shows a photograph of a test platform from 1958 where researchers used a rotational encoder on a reel of taught cable to measure the relative distance and relative velocities between two vehicles (in lieu of a radar sensor). Data was collected using an oscillograph and the pedal controllers were based on purely analog circuitry.

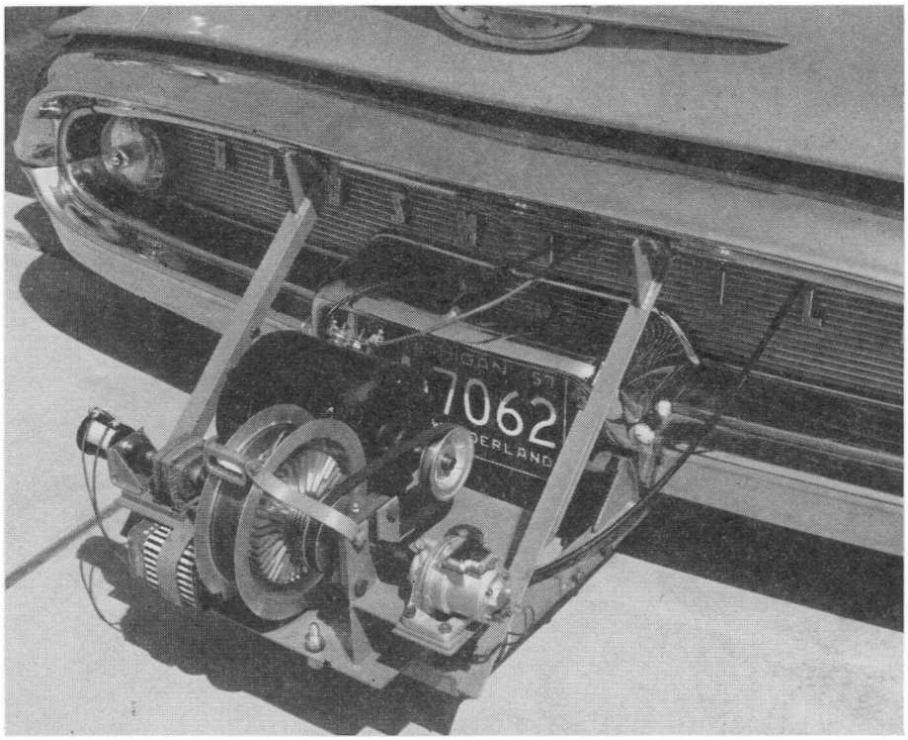

Figure 1.1: Photograph showing the mechanism used to measure relative velocity and distance in early works. Reproduced from [4] with permission.

These early efforts on car following [4] simply attempted to replicate human driving behavior. Modern approaches to platooning focus on achieving small inter-vehicle spacing that may be infeasible for human drivers as this has been demonstrated to improve traffic throughput (mobility) as well as reduce fuel consumption [5, 6]. At the same time, a sufficient headway has to be

maintained between vehicles to prevent pile-ups. Consequently, a majority of contemporary research on vehicle platooning involves achieving the smallest possible inter-vehicle spacing while guaranteeing safety.

To ensure safety in a vehicle platoon, any disturbances that occur at the head of a platoon need to dampen out as it propagates towards the tail. This condition is referred to as string stability. A more formal definition will be discussed later.

Adaptive Cruise Control (ACC) systems are now widely available on passenger vehicles. These use onboard sensors (typically radar) to measure the relative velocity and distance to the preceding vehicle. This information is then used in a servomechanism to supply throttle or brake input to the ego vehicle for vehicle platooning. Cooperative Adaptive Cruise Control (CACC) systems utilize additional information (typically acceleration) transmitted directly from the preceding vehicle using wireless Vehicle-to-Vehicle (V2V) communication. Advanced cooperative systems implement more complex communication typologies and can utilize information from multiple preceding or succeeding vehicles. For the purpose of this work, ACC refers to the control scheme that is restricted to using on-board information, CACC refers to a scheme that utilizes acceleration information from the immediate vehicle ahead and CACC+ refers to a platoon system that utilizes acceleration measurements from both the vehicles ahead. For clarity, Figures 1.2 and 1.3 provide a visualization of the information flow for CACC and CACC+ systems. These figures were reproduced from [7].

Figure 1.2: CACC platoon using information from one immediately preceding vehicle. Reprinted with permission from [7]

It has been long established that for an ACC platoon, string stability can be guaranteed if the

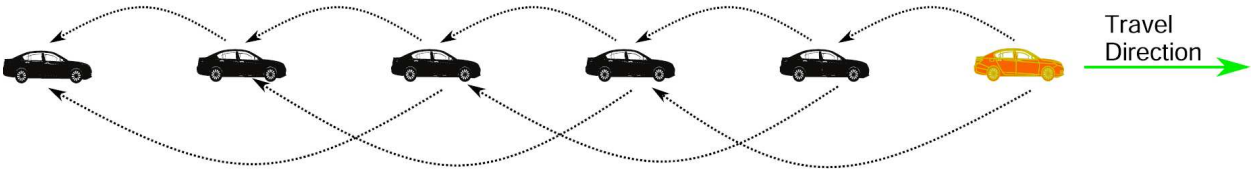

Figure 1.3: CACC+ platoon using information from two preceding vehicles. Reprinted with permission from [7]

time headway chosen is at least twice the sum of parasitic lags in the vehicle, assuming homogeneity in vehicle capabilities [8] . It has also been demonstrated that the time headway can be safely reduced further in CACC platoons using V2V communication [9]. Majority of early work on vehicle platooning ignored imperfections in the V2V links. In reality, wireless channels are prone to packet drops due to interference and/or bandwidth restrictions. In the last decade, researchers have noted that lossy communication channels degrade string stability [10, 11]. Workarounds have also been proposed [12, 13] that estimate the information lost due to dropped packets. Nevertheless, the algorithm in [12] does not account for the packet loss rate and consequently enforces a significant penalty on the time headway even if only a few packets are dropped. While [13] suggests that the minimum stabilizing time headway increases with packet loss rates, it does not provide an express relationship between headway and the effective loss rate. Moreover, both of them enforce additional computational burden as they require implementing an estimator.

We should note that some researchers have focused on delays in the platoon instead of lags [14–16]. Zeng et al [17] have also studied stochastic communication delays in platoons and derived bounds on the maximum allowable delay for string stability. That said, the latest test reports from the 5G Automotive Association have concluded that the end-to-end latency for platooning applications remained under 100 ms [18] in spite of heavy congestion (over 500 vehicles contributing to interference). On the other hand, we measured the lag in deceleration of a 2017 Lincoln MKZ to be over 370 ms and our own testing revealed communication latency in a non-congested scenario to be well under 5 ms. Consequently, we have assumed the vehicle model to be dominated by actuation lags rather than delays. Moreover, packet loss phenomenon is more common [19] due to

loss of Line-Of-Sight in V2V applications, so it is more likely that a packet will be lost completely rather than arrive with a delay.

Our approach also has an advantage over works like [11], [17] which appear to incorrectly conclude that if network performance is poor, string stability cannot be achieved. Our approach allows smooth (and reversible) transition from CACC+, to CACC and then to ACC (no communication) depending on the packet reception performance.

Finally, we re-examine the notion of string stability from a practical perspective. For a platoon to be string stable, any fluctuations that occur at the head of a platoon need to be damped out as they propagate towards the tail. This condition is often expressed in the frequency domain [8] which ensures that the 2-norm of spacing errors (i.e., the power of spacing error signals) do not amplify. However from a safety perspective, it is the maximum (infinity norm) of the spacing error signal that dictates if a collision will occur. A further discussion of this issue is presented in [7]. In the current work, we develop an upper bound for the maximum spacing error as a function of the acceleration maneuver of the lead vehicle. This result, presented for both CACC and CACC+ schemes [20] can also be used to pick a safe standstill distance, which many previous works either ignore (set to zero) or pick arbitrarily. Ignoring the standstill distance is not practical as it would mean that the bumpers of vehicles touch when the vehicles are stationary. At the same time, arbitrarily choosing this parameter risks an unnecessary increase in inter-vehicular spacing which needs to be minimized as much as possible, for improved fuel efficiency and mobility.

To summarize, the three main contribution of this dissertation on the topic of vehicle platooning are as follows:

- Provide a sufficient condition on the minimum string stable time headway for platoons with lossy V2V communication.
- Demonstrate the validity of the proposed lossy vehicle follower systems through high fidelity numerical simulations.
- Develop a usable bound on the maximum spacing error in a homogeneous platoon, which is

more germane to safety and collision prevention compared to traditional criterion for string stability.

Chapter 2 presents the vehicle and wireless channel models used and Chapter 3 presents the derivation of minimum time headway for lossy CACC platoons and extension to multiple vehicle lookup schemes. In Chapter 4, simulations and experiments with a real-vehicle are presented to corroborate the results on lossy platooning. Finally, Chapter 5 presents the discussion on the upper bound of the maximum spacing error in a platoon. Many of the figures and portions of the text in these chapters have been reproduced (with permission) from the papers that were published over the course of this study [7, 20–22].

1.2 Object Tracking in Adverse Visibility Conditions

It is well known that over 90% of traffic accidents on roads are caused by human errors [1, 2]. The primary goal of fully autonomous driving is to eliminate such accidents by removing the driver from the equation. For such vehicles to operate safely, they need to be able to perceive other road users (cars, bikes, pedestrians, etc.) as well as, if not better than, a human driver. Currently, no single sensor exists on the market that can perform this task by itself. Instead, autonomous driving systems utilize a combination of sensors for perceiving the environment

Radars, first developed for military and aviation applications, are used for measuring distance and speed of objects. They have been used by automotive manufacturers in the last couple of decades for implementing adaptive cruise control and collision avoidance/emergency braking features. The primary drawback of automotive radars is the low spatial resolution and consequently, their inability to distinguish the type of obstacle ('object classification') from measurements. Lidars, or laser scanners, offer better angular resolution and consequently enable better object classification, especially when combined with neural network based approaches [23, 24]. Cameras yield the highest resolution and are usually designed to work in the visible range (400 to 700 nanometers). Digital cameras typically output color information in three channels (Red, Green Blue - 'RGB') for each pixel and are best suited for object classification.

A fully autonomous vehicle, as defined by Society of Automotive Engineers, must be able to

perform all driving functions (including perception) under all conditions [25]. In order to achieve Level 5 autonomy we need to design systems that work reliably even in adverse weather and visibility conditions, without the need for human intervention.

While RGB cameras have the highest resolution, they yield limited information at night due to low lighting. They can only sense the area covered by the headlights/streetlights and are further hindered by headlight bloom from oncoming vehicles. Moreover, they are severely disrupted by direct glare while driving directly in the direction of sunrise or sunset, as shown in Figure 1.4.

Loss of visibility under intense sunlight can be fatal, as demonstrated by the failure of Tesla's AutoPilot system to detect the side of a trailer in 2016 [26]. Recently, [27] presented an approach for improving visibility in direct sunlight by using a High Dynamic Range (HDR) camera that captures multiple frames at different exposure settings to create a composite image. Apart from adding additional computational expense, the same approach is not guaranteed to work for night-time autonomous driving and may not allow high frame rates.

Thermal cameras, especially those operating over the Long Wavelength Infrared (LWIR) spectrum (8000 to 14,000 nanometers) are inherently resilient to direct sunlight, as demonstrated in Figure 1.5, which presents the same scene as in Figure 1.4, but as seen from a thermal camera. Moreover, a study by [28] demonstrated the superior performance of LWIR cameras over lidars and RGB cameras in foggy conditions for identifying pedestrians.

Consequently, in the second part of this thesis, we propose an object detection and tracking system that utilizes thermal cameras in combination with an automotive radar to complete the perception task in adverse visibility conditions.

In Chapter 6, we present details of the sensor packs used and the data collection strategy. Chapter 7 describes the data association algorithm used for processing measurements from the cameras and radar, followed by results and validation in Chapter 8. Some of the figures have been reproduced with permission from one of our previously published papers [29].

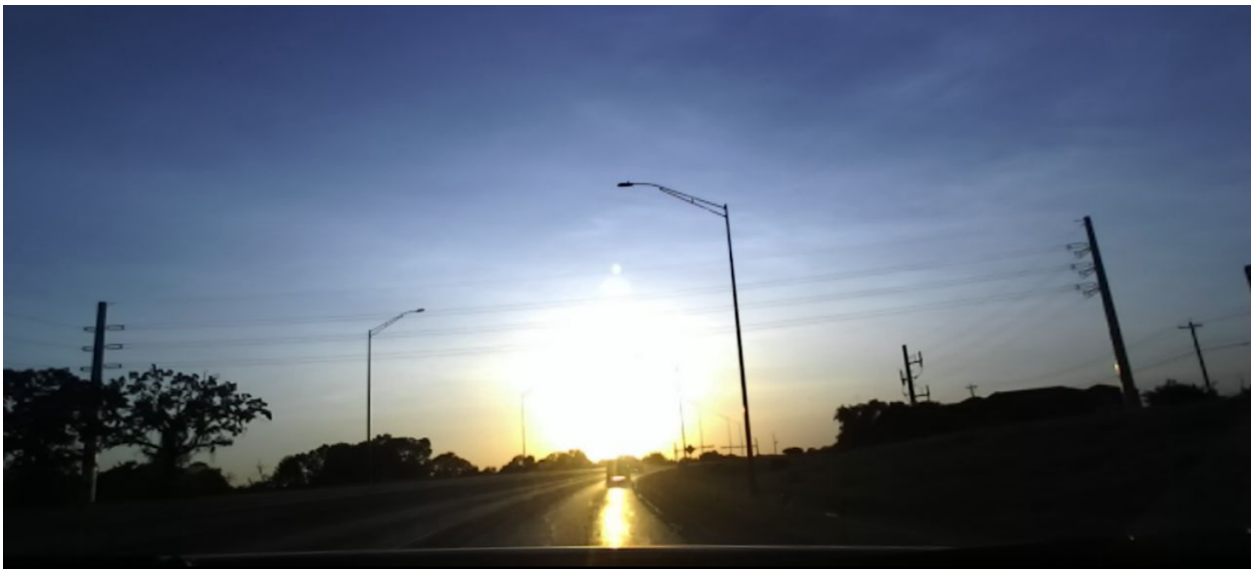

Figure 1.4: RGB camera hindered by direct sunlight, taken with a ZED camera. Reprinted with permission from [29]. ©SAE International.

Figure 1.5: Thermal cameras are resilient to direct sunlight. Reprinted with permission from [29]. ©SAE International.

In this chapter, we will develop the equations of motion for the vehicle platoon, define the controllers and the communication channels that will be used in later chapters.

2.1 Vehicle Model and Control Law

Hydraulic and pneumatic braking systems used in automobiles take time to build up pressure on the brake calipers after the brake pedal is depressed. This effect is more pronounced in heavy vehicles with pneumatic brakes but is still measurable in passenger vehicles. Please note that we are not taking about the dead-band/delay in the system (which is usually much smaller) but the rise time to achieve maximum deceleration rate.

These parasitic lags can be represented as τ. Let us suppose there is one lead vehicle and N follower vehicles in the platoon. We will denote the platoon leader with index 0. Other vehicles are indexed as shown in figure 2.1. For studying string stability, we model vehicles as point masses

Figure 2.1: Figure showing vehicle indexing scheme

whose acceleration can be controlled through first order actuation dynamics:

$$\ddot{x}_i = a_i, \quad \tau \dot{a}_i + a_i = u_i, \tag{2.1}$$

where u_i is the control input for the i^{th} vehicle and x_i is its position. While the lag in individual vehicles of the platoon may vary, it is reasonable to assume that it is bounded above by some value for all vehicles. We will use this upper bound as the maximum lag τ for the platoon. In

this way, any heterogeneity in the parasitic lags in the platoon can be accounted for. We note that such models have been used successfully in experiments conducted in the California PATH projects [30, 31].

We can now define the spacing error for the i^{th} vehicle as:

$$e_i := x_i - x_{i-1} + d + h_w v_i, \tag{2.2}$$

where h_w is the time headway employed in the platoon. Thus, the control law for the i^{th} vehicle for a CACC platoon with one-vehicle lookup policy is written as:

$$u_i = K_a a_{i-1} - K_v(v_i - v_{i-1}) - K_p(x_i - x_{i-1} + h_w v_i), \tag{2.3}$$

where K_a, K_v, K_p are tunable gains. Similarly, for a two-vehicle lookup scheme, it takes the form:

$$\begin{aligned} u_i = {} & K_a a_{i-1} - K_v(v_i - v_{i-1}) - K_p(x_i - x_{i-1} + d + h_w v_i) \\ & + K_a a_{i-2} - K_v(v_i - v_{i-2}) - K_p(x_i - x_{i-2} + 2d + 2h_w v_i) \end{aligned} \tag{2.4}$$

2.2 Wireless Communication Channel

Since a forward facing radar sensor mounted on a follower car can be used to measure the relative velocity (through Doppler shift) and relative distance (using time of flight), the only information that needs to be transmitted wirelessly for a CACC policy is the preceding vehicle's acceleration (a_{i-1}). For a CACC+ policy in eq. (2.4) the relative position and velocity terms associated with the $(i-2)^{th}$ vehicle cannot be measured by radar due to lack of line of sight. So instead, the whole state of the second preceding vehicle needs to be transmitted.

Let us define $\hat{w}_{i,i-j}$ as the stochastic variable that represents whether a packet was successfully received by the i^{th} vehicle from the $(i-j)^{th}$ vehicle for $j = 1, 2, 3 \ldots$, where each $\hat{w} \in \{0, 1\}$. For example, if a packet is received successfully by the i^{th} from the immediately preceding $(i-1)^{th}$ vehicle, then $\hat{w}_{i,i-1} = 1$; otherwise it takes the value 0. Then, each of the ideal control laws can

be replaced by a stochastic equation with a random variable associated with each communication link.

For a lossy CACC system, we have:

$$\tau \dot{a}_i + a_i = \hat{w}_{i,i-1} K_a a_{i-1} - K_v(v_i - v_{i-1}) - K_p(x_i - x_{i-1} + d + h_w v_i). \tag{2.5}$$

For a lossy two vehicle lookup (CACC+), we have:

$$\begin{aligned}\tau \dot{a}_i + a_i = \hat{w}_{i,i-1} K_a a_{i-1} - K_v(v_i - v_{i-1}) - K_p(x_i - x_{i-1} + d + h_w v_i) \\ + \hat{w}_{i,i-2}\{K_a a_{i-2} - K_v(v_i - v_{i-2}) - K_p(x_i - x_{i-2} + 2d + 2h_w v_i)\},\ \forall i \geq 2.\end{aligned} \tag{2.6}$$

Please note that the first following vehicle ($i = 1$) in a lossy CACC+ platoon only has one predecessor and will hence use eq. (2.5) as its control law.

Now, each $\hat{w}$ can be modeled as an *i.i.d* (independent, identically distributed) variable, but in reality successive packet drops are not independent. A burst-noise channel model for bit errors was introduced in 1960 by E. N. Gilbert [32]. Since then, it has been widely used (along with some of the model's extensions [33, 34]) to simulate bursts of noise and packet drops in wireless channels. In its simplest form, the Gilbert model can be described as a two-state system as shown in Fig. 2.2. The input to the wireless channel in our case is the acceleration of the preceding vehicle. In the 'Good' state, there are no packets dropped and the input information is transmitted successfully. In the 'Bad' state, only $R\%$ of the packets are transmitted successfully. Further, the transition probabilities from 'Good'$\rightarrow$'Bad' and 'Bad'$\rightarrow$'Good' are P and Q respectively. P and Q are typically small so the states tend to persist for a few transmission cycles, imparting burst behavior to the channel. In fact, we can now see that the *i.i.d* packet drop behavior is a special case of the Gilbert model with only one 'Bad' state where successful packet reception occurs with some probability. Since errors only occur in the dropped state, we can calculate the average packet reception rate which we denote as γ.

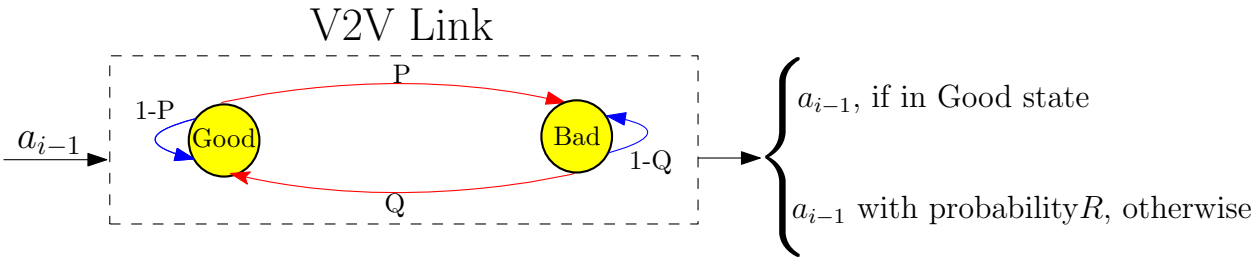

Figure 2.2: Transmission diagram for wireless link between the i^{th} and $(i-1)^{th}$ vehicle. Reprinted with permission from [20]. ©2021 IEEE.

$$\mathbb{E}[\hat{w}] = 1 - \frac{P(1-R)}{P+Q} =: \gamma, \tag{2.7}$$

It should be noted that in practice, average packet reception rate, γ can be locally measured by the receiver if transmission rate is fixed (as can be expected from real-time systems) and known before hand (either by design or as part of an eventual V2V standard). The choice of interval used for updating γ can be left to the designer based on the transmission bandwidth available.

3. AVFS: MINIMUM TIME HEADWAY

As mentioned in Chapter 1, packet drops in the communication link can affect string stability (and consequently the minimum employable time headway). Therefore, it is necessary to adjust the time headway in the presence of packet losses, if collisions are to be avoided. As part of the supplementary material for this thesis, a video simulation showing the effect of 25% packet drops on a vehicle platoon is available to view online[1], to serve as a visual proof for the motivation .

In this chapter, we will try to determine the minimum string stable time headway for vehicle platoons with lossy communication channels.

3.1 Convergence of State Vector for Lossy CACC

First, we will show using induction that when a large number of realizations of the stochastic system (2.5) are taken, the average approaches a known deterministic equivalent. This deterministic system will then be used to obtain the minimum string stable time headway. This induction procedure for lossy CACC has been duplicated from our recent conference paper [20] for completeness as we will refer to it again for the CACC+ case in the next section.

We will operate under the assumption that the communication link between any pair of vehicles is independent from any other pair. This is largely true in non-congested scenarios. Admittedly, this simplification was necessary to maintain tractability of the problem. Moreover, similar assumptions of independence have been used successfully by other researchers [17, 35].

Suppose there are k vehicles in the platoon operating with the stochastic control law in (2.5). We can consider γ for the platoon to be the smallest among those measured over the individual V2V links. Let u_L be the input imparted to the lead vehicle. The stochastic system of the entire platoon can be written in the state space form as:

$$\dot{\hat{X}} = \hat{A}(\hat{w}(t))\hat{X} + BU, \tag{3.1}$$

[1] https://youtu.be/BBCDDttpkIU

where $\hat{X}$=$(x_0, v_0, a_0, x_1, v_1, a_1, \cdots x_k, v_k, a_k)$ and $U = u_L$, the input to the lead vehicle. Note that only the system matrix $\hat{A}(\hat{w}(t))$ has random elements. For sake of clarity, we have provided an example of $\hat{A}$ and B using equation (2.5) for a three (1 lead, 2 following) vehicle CACC platoon with imperfect (lossy) V2V communication. The two random entries in the 9×9 system matrix are highlighted.

$$\hat{A}_L = \begin{bmatrix} 0 & 1 & 0 & & & & & & \\ 0 & 0 & 1 & & & & & & \\ 0 & 0 & \frac{-1}{\tau} & & & & & & \\ & & & 0 & 1 & 0 & & & \\ & & & 0 & 0 & 1 & & & \\ \frac{K_p}{\tau} & \frac{K_v}{\tau} & \frac{\hat{w}_{1,0}K_a}{\tau} & \frac{-K_p}{\tau} & p_1 & \frac{-1}{\tau} & & & \\ & & & & & & 0 & 1 & 0 \\ & & & & & & 0 & 0 & 1 \\ 0 & 0 & 0 & \frac{K_p}{\tau} & \frac{K_v}{\tau} & \frac{\hat{w}_{2,1}K_a}{\tau} & \frac{-K_p}{\tau} & p_1 & \frac{-1}{\tau} \end{bmatrix},$$

$$B_L = \begin{bmatrix} 0 & 0 & 1 & 0 & 0 & 0 & 0 & 0 & 0 \end{bmatrix}^T, \tag{3.2}$$

where

$$p_1 = -\frac{K_v + K_p h_w}{\tau}.$$

Let Δt be the controller time step so that the total (finite) run time is $t_m = m\Delta t$, $m \in \mathbb{N}$. Let us consider the evolution of the stochastic state vector over the first time interval $[0, t_1)$:

$$\hat{X}(t_1) = \hat{\Phi}(t_1, 0)\hat{X}(0) + \int_0^{t_1} \hat{\Phi}(t_1, \zeta)BU(\zeta)d\zeta, \tag{3.3}$$

where $\hat{\Phi}(t_1, 0)$ is the stochastic state transition matrix, dependent on the values of $\hat{w}_{i,j}$ at $t = 0$. In

implementation, the control input U would only be updated at the beginning of each time step so it can be considered constant over the duration of each interval.

Since we have defined $\mathbb{E}[\hat{w}_{i,j}] = \gamma$, let us consider replacing the random elements in the system matrix of equation (3.1) with their expected values. Then we get some deterministic system:

$$\dot{\bar{X}} = \bar{A}\bar{X} + BU \tag{3.4}$$

Our goal now is to show that $\mathbb{E}[\dot{\hat{X}}(t)] = \dot{\bar{X}}(t)$, for all $t \in [0, t_m]$. For the deterministic system, the state evolution for the first interval $[0, t_1)$ is:

$$\bar{X}(t_1) = \bar{\Phi}(t_1, 0)\bar{X}(0) + \int_0^{t_1} \bar{\Phi}(t_1, \zeta)d\zeta BU(0). \tag{3.5}$$

Now consider $\hat{\Phi}(t_1, 0)$ and $\bar{\Phi}(t_1, 0)$. Since $\hat{A}(\hat{w}(t))$ only changes at each controller time step, it is constant in the interval $[0, t_1)$ and retains the value from the beginning of the interval $\hat{A}(\hat{w}(0)) =: \hat{A}_1$. So, we can write

$$\hat{\Phi}(t_1, 0) = e^{\int_0^{t_1} \hat{A}(\hat{w}(\xi))d\xi} = e^{\hat{A}_1 t_1} \tag{3.6}$$

$$\bar{\Phi}(t_1, 0) = e^{\int_0^{t_1} \bar{A}d\xi} = e^{\bar{A}t_1} \tag{3.7}$$

Now we use the power series expansion for the exponential matrices:

$$e^{\hat{A}_1 t_1} = I + \hat{A}_1 t_1 + \frac{(\hat{A}_1 t_1)^2}{2!} + \frac{(\hat{A}_1 t_1)^3}{3!} + \cdots \tag{3.8}$$

$$e^{\bar{A}t_1} = I + \bar{A}t_1 + \frac{(\bar{A}t_1)^2}{2!} + \frac{(\bar{A}t_1)^3}{3!} + \cdots \tag{3.9}$$

While generally not true for random matrices [36], the following is true for CACC system matrices with one vehicle lookup case given in equation (3.2):

Theorem 1.

$$\mathbb{E}[\hat{A}_1^n] = \bar{A}^n, \quad \forall n \in \mathbb{N} \tag{3.10}$$

Proof of this theorem is given in the Appendix A. The Proof for this theorem holds due to the property of matrix A in our case, since the diagonal elements of the system matrix are purely deterministic and the powers of $\hat{A}$ only contain elements that are multi-linear in $\hat{w}_{i,j}$. This allows us to exploit the fact that the expectation of a product of independent random variables is the product of their expectations. We have noticed that this convenient multi-linear property of the powers of system matrices is afforded only for one vehicle lookup schemes (CACC) but not for platoons that utilize communicated information from two or more preceding vehicles (CACC+ systems), as discussed in Section 3.2.

Thus, over a large number of realizations,

$$\mathbb{E}[\hat{\Phi}(t_1, 0)] = \bar{\Phi}(t_1, 0). \tag{3.11}$$

Since the initial conditions can be assumed to be the same in equations (3.3) and (3.5), i.e., $\hat{X}(0) = \bar{X}(0)$, we get:

$$\mathbb{E}[\hat{X}(t_1)] = \bar{X}(t_1), \tag{3.12}$$

for the first interval $[0, t_1)$. Let this form the base case with the induction hypothesis for interval $[t_{k-1}, t_k)$ as:

$$\mathbb{E}[\hat{X}(t_k)] = \bar{X}(t_k) \tag{3.13}$$

Now consider the next interval $[t_k, t_{k+1})$

$$\hat{X}(t_{k+1}) = \hat{\Phi}(t_{k+1}, t_k)\hat{X}(t_k) + \int_{t_k}^{t_{k+1}} \hat{\Phi}(t_{k+1}, \zeta)d\zeta BU(t_k)$$
$$\bar{X}(t_{k+1}) = \bar{\Phi}(t_{k+1}, t_k)\bar{X}(t_k) + \int_{t_k}^{t_{k+1}} \bar{\Phi}(t_{k+1}, \zeta)d\zeta BU(t_k)$$

Using a similar reasoning as in equations (3.6) - (3.11), we can show that $\mathbb{E}[\hat{\Phi}(t_{k+1}, t_k)] = \bar{\Phi}(t_{k+1}, t_k)$.

Again, note that the term $\hat{\Phi}(t_{k+1}, t_k)\hat{X}(t_k)$ only contains products of independent random variables. From the induction hypothesis in equation (3.13), we can claim $\mathbb{E}[\hat{\Phi}(t_{k+1}, t_k)\hat{X}(t_k)] = \bar{\Phi}(t_{k+1}, t_k)\bar{X}(t_k)$. This yields:

$$\mathbb{E}[\hat{X}(t_{k+1})] = \bar{X}(t_{k+1}). \tag{3.14}$$

From the principle of mathematical induction, $\mathbb{E}[\hat{X(t)}] = \bar{X}(t)$ for all finite $t \in [0, t_m]$. This allows us to replace equation (2.5) with its deterministic equivalent.

$$\tau\dot{a}_i + a_i = \gamma K_a a_{i-1} - K_v(v_i - v_{i-1}) - K_p(x_i - x_{i-1} + d + h_w v_i) \tag{3.15}$$

Following the procedure in [9] for this governing equation, we obtain the bound on the minimum employable time headway.

$$h_w \geq h_{min} = \frac{2\tau}{1 + \gamma K_a} \tag{3.16}$$

3.2 Multiple Predecessor Lookup Scheme

First let us consider a two vehicle lookup scheme with packet losses. The equation of motion for each vehicle in the platoon is given by:

$$\tau \dot{a}_0 + a_0 = u_L \tag{3.17}$$

$$\tau \dot{a}_1 + a_1 = \hat{w}_{1,0} K_a a_0 - K_v(v_1 - v_0) - K_p(x_1 - x_0 + d + h_w v_1) \tag{3.18}$$

$$\begin{aligned} \tau \dot{a}_i + a_i = {} & \hat{w}_{i,i-1} K_a a_{i-1} - K_v(v_i - v_{i-1}) - K_p(x_i - x_{i-1} + d + h_w v_i) \\ & + \hat{w}_{i,i-2}\{K_a a_{i-2} - K_v(v_i - v_{i-2}) - K_p(x_i - x_{i-2} + 2d + 2h_w v_i)\}, \ \forall i \geq 2. \end{aligned} \tag{3.19}$$

The above system is stochastic, and we would like to obtain a deterministic equivalent of the system in order to derive a sufficient condition for a string stable time headway that can be deployed over lossy communication channels. The stochastic system can be expressed in a similar state space form as in equation (3.1). For clarity, $\hat{A}(\hat{w}(t))$ is provided for a (2+1) vehicle platoon, with the last vehicle using acceleration information from the second and full state information from leading vehicle. It should be stressed that unlike the CACC case, the position and velocity information of the $(i-2)^{th}$ vehicle cannot be measured using onboard sensors on the ego (i^{th}) vehicle, so they are transmitted wirelessly along with the acceleration information. Again, the random entries in the matrix are highlighted.

$$A_2 = \begin{bmatrix} 0 & 1 & 0 & & & & & & \\ 0 & 0 & 1 & & & & & & \\ 0 & 0 & \frac{-1}{\tau} & & & & & & \\ & & & 0 & 1 & 0 & & & \\ & & & 0 & 0 & 1 & & & \\ \frac{K_p}{\tau} & \frac{K_v}{\tau} & \frac{\hat{w}_{1,0}K_a}{\tau} & \frac{-K_p}{\tau} & P_1 & \frac{-1}{\tau} & & & \\ & & & & & & 0 & 1 & 0 \\ & & & & & & 0 & 0 & 1 \\ \frac{\hat{w}_{2,0}K_p}{\tau} & \frac{\hat{w}_{2,0}K_v}{\tau} & \frac{\hat{w}_{2,0}K_a}{\tau} & \frac{K_p}{\tau} & \frac{K_v}{\tau} & \frac{\hat{w}_{2,1}K_a}{\tau} & P_2 & P_3 & \frac{-1}{\tau} \end{bmatrix}$$

$$B_L = \begin{bmatrix} 0 & 0 & 1 & 0 & 0 & 0 & 0 & 0 & 0 \end{bmatrix}^T, \tag{3.20}$$

where

$$\begin{aligned} P_1 &= -\frac{K_v + K_p h_w}{\tau} \\ P_2 &= -\frac{K_p + \hat{w}_{2,0} K_p}{\tau} \\ P_3 &= -\frac{K_v + K_p h_w + \hat{w}_{2,0}(K_v + 2K_p h_w)}{\tau} \end{aligned} \tag{3.21}$$

Suppose we attempt to use a similar approach to that presented in section 3.1, we see that the powers of $\hat{A}_2$ matrix are no longer multi-linear in the random elements. Consequently,

$$\mathbb{E}[\hat{A_2}^n] \neq \bar{A_2}^n, \qquad \forall n \geq 3,$$

which renders the earlier approach futile.

The task of obtaining an exact deterministic equivalent of eqs. (3.17) to (3.19) in essence, can

be represented as follows:

Given a random matrix S whose elements are not necessarily independent of each other, find a deterministic matrix D such that:

$$\mathbb{E}[e^S] = e^D \tag{3.22}$$

To the best of our knowledge, finding an exact expression for D appears to be tedious for non-trivial cases. While a wealth of results are available in random matrix theory, they either rely on diagnonalizability of the matrix or independence of its elements [37, 38]. S. Geman and R. Khasminskii [39, 40] provide some results on convergence of stochastic differential equations, but they appear to require infinitesimally small time steps, which is not practical for implementation on real vehicles. A brute force computational method can be pursued where the matrix exponential of a large number of realizations of the e^S matrix are taken and averaged to get e^D. Then its matrix logarithm needs to be calculated numerically to obtain D. We observed a significant loss of precision due to the multiple floating point operations involved in taking matrix exponentials. This causes difficulty in finding a real valued matrix logarithm.

While finding an exact deterministic expression is difficult, we propose the following approximation for the system, by replacing all random variables with their expectations.

$$\tau\dot{a}_0 + a_0 = u_L \tag{3.23}$$

$$\tau\dot{a}_1 + a_1 = \gamma K_a a_0 - K_v(v_1 - v_0) - K_p(x_1 - x_0 + d + h_w v_1) \tag{3.24}$$

$$\begin{aligned}\tau\dot{a}_i + a_i = {} & \gamma K_a a_{i-1} - K_v(v_i - v_{i-1}) - K_p(x_i - x_{i-1} + d + h_w v_i) \\ & + \gamma\{K_a a_{i-2} - K_v(v_i - v_{i-2}) - K_p(x_i - x_{i-2} + 2d + 2h_w v_i)\},\ \forall i \geq 2\end{aligned} \tag{3.25}$$

To understand the behavior of this approximated deterministic system compared to the stochastic system, we simulated 100 realizations of a 10 vehicle stochastic platoon during an emergency

braking scenario. Time step used in all the simulations was 0.01 s. Transition probabilities for the Gilbert channel from Fig 2.2 were picked as $P = 0.2, Q = 0.1, R = 0.2$. All 100 stochastic spacing error trajectories of the 10^{th} vehicle are shown in Fig. 3.1, along with their average. The corresponding spacing error trajectory from the proposed system is also shown in the same figure. While we know that eqs. (3.23) to (3.25) are not the deterministic equivalent of eqs. (3.17) to (3.19), we can see that the difference in peaks between the proposed and average trajectories is relatively small (in this case, 0.21 m, less than 5% of the peak value). So for the purpose of developing an analytical bound for the minimum string stable time headway, we will proceed with eqs. (3.23) to (3.25). We will use the definition of spacing error from eq. (2.2).

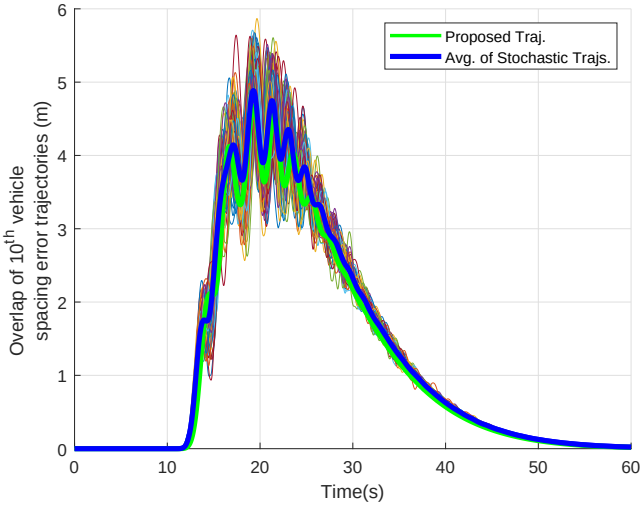

Figure 3.1: Overlaid stochastic spacing error trajectories and the proposed approximation. Reprinted with permission from [20]. ©2021 IEEE.

After some algebraic manipulation, we obtain the following equation of motion for each of the

i^{th} following vehicle, for $i \geq 2$:

$$\begin{aligned}\tau\dddot{e}_i + \ddot{e}_i = \quad & K_p e_{i-1} - K_p e_i - K_v \dot{e}_i - \gamma K_v \dot{e}_i - K_p h_w \dot{e}_i \\ & + K_v \dot{e}_{i-1} + \gamma K_p e_i + \gamma K_a \ddot{e}_{i-1} + \gamma K_a \ddot{e}_{i-2} \\ & + \gamma K_v \dot{e}_{i-2} + \gamma K_p e_{i-2} + 2\gamma K_p h_w \dot{e}_i \end{aligned} \tag{3.26}$$

This can be written in the Laplace domain as:

$$E_i(s) = H_{p1} E_{i-1}(s) + H_{p2} E_{i-2}(s) \tag{3.27}$$

where

$$\begin{aligned} & H_{p1}(s) \\ & = \frac{\gamma K_a s^2 + K_v s + K_p}{\tau s^3 + s^2 + s[(1+\gamma)K_v + (1+2\gamma)K_p h_w] + (1+\gamma)K_p} \end{aligned} \tag{3.28}$$

and

$$\begin{aligned} & H_{p2}(s) \\ & = \frac{\gamma K_a s^2 + \gamma K_v s + \gamma K_p}{\tau s^3 + s^2 + s[(1+\gamma)K_v + (1+2\gamma)K_p h_w] + (1+\gamma)K_p} \end{aligned} \tag{3.29}$$

We can obtain minimum required time headway h_{min} for the lossy CACC+ platoon by taking the maximum of the two yielded from $H_{p1}(s)$ and $H_{p2}(s)$, by using Theorem 1 in [9]. Thus, the sufficient condition on time headway for two vehicle lookup is:

$$h_w \geq h_{min} = \quad \frac{2\tau(1+\gamma)}{(1+2\gamma)(1+\gamma(1+\gamma)K_a)} \tag{3.30}$$

Please note that in equations eqs. (3.23) to (3.25), we have assumed that the expectations are all equal to γ. It is possible that $\hat{w}_{2,0}$ may have a significantly different value from that of $\hat{w}_{1,0}$ or $\hat{w}_{2,1}$ due to poor line-of-sight (since there is a vehicle in between). In that case, we can consider $\mathbb{E}[\hat{w}_{2,0}] = \mu$ and $\mathbb{E}[\hat{w}_{1,0}] = \mathbb{E}[\hat{w}_{2,1}] = \gamma$. The latter equality can be enforced by picking the minimum of the individually measured packet reception rates, which should be close to each other since they both have direct line of sight of the preceding vehicle. Then, the limit can be obtained from similar algebra:

$$h_w \geq h_{min} = \quad \frac{2\tau(1+\mu)}{(1+2\mu)(1+\gamma(1+\mu)K_a)} \tag{3.31}$$

Similarly, the minimum time headway for a lossy three-vehicle lookup policy can be derived and is presented in Appendix B.

Finally, we can extend this to a generalized r-vehicle lookup scheme. Let us define

$$\mathbb{E}[\hat{w}_{i,i-j}] =: \gamma_j$$

where, $\gamma_j, j = 1, 2, 3 \cdots$ is the packet reception probability of the link between any vehicle i and its j^{th} predecessor. After some algebra, we can derive the minimum string stable time headway for a lossy r-vehicle lookup policy:

$$h_{min} \geq \frac{2\tau(1+\sum_{j=2}^{r}\gamma_j)}{(1+\sum_{j=2}^{r}j\gamma_j)[1+\gamma_1(1+\sum_{j=2}^{r}\gamma_j)K_a]}.$$

We can show that in the case of perfect (lossless) communication, above equation elegantly reduces to the known result from [9] with $\gamma_j = 1$, for all j.

$$h_{min} \geq \frac{4\tau}{(r+1)(1+rK_a)}$$

4. AVFS: SIMULATIONS AND EXPERIMENTS

The ideal method to corroborate the bound on minimum time headway is to implement the controller on four or more passenger cars and perform real-world experiments, which is logistically demanding. Also, it would be expensive to demonstrate string instability under emergency braking scenarios with multiple real vehicles. Instead, we first develop longitudinal model of a 2017 Lincoln MKZ using throttle and brake maps. Once the model is validated using experimental data, we implement six virtual vehicles in Simulink to demonstrate the advantages of the proposed algorithm. As a preliminary check, we first perform simulations using the linear point mass model from equation (2.1).

Finally, we present real-world tests with control law developed earlier for a lossy one-vehicle lookup policy using the same Lincoln MKZ with a virtual lead vehicle.

4.1 Preliminary Simulations with Point Mass model

We will simulate a homogeneous platoon with actuation lag $\tau = 0.4s$ using Simulink. Transition probabilities for the Gilbert channel from Fig. 2.2 were picked as: $P = 0.2, Q = 0.1, R = 0.2$. This yields $\gamma = 0.467$ from equation (2.7). Here, we will consider a CACC+ platoon of seven (one lead + six follower) vehicles using the control scheme given in eqs. (3.17) to (3.19). For simulations with the same linear model with one-vehicle lookup, please refer to [21, 22]. For CACC+, the first following vehicle only has one predecessor so it uses the CACC control law from equation (2.5).

The lead vehicle's maneuver is as follows: At the start of the simulation, it is moving with a velocity of 25 m/s, then at $t = 10$ s, it decelerates at the rate of -9 m/s^2 to 16 m/s. This velocity is maintained for the remaining duration of the simulation. In all the following simulations, we assume that the platoon is in steady state at the start of each run. This setup is similar to an emergency braking maneuver. Controller gains were chosen as follows: $(K_a, K_v, K_p) = (0.2, 2.5, 1)$. Spacing error trajectories for the 1^{st}, 3^{rd} and 5^{th} follower vehicles for three different communication

scenarios are presented in Fig. 4.1.

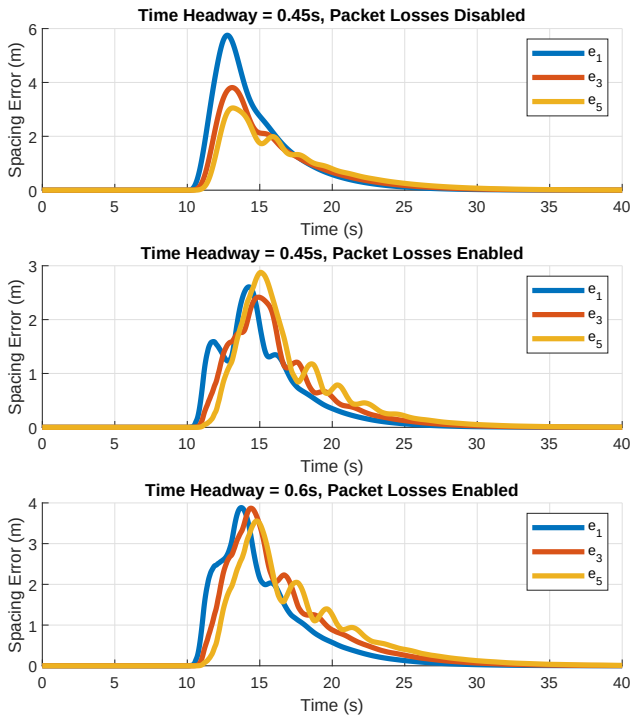

Figure 4.1: Spacing errors a CACC+ platoon with linear point mass model under different scenarios. Reprinted with permission from [20]. ©2021 IEEE.

First, the platoon is simulated with a time headway of 0.45 s but with no packet losses. This scenario is expected to result in a string stable platoon, since the headway exceeds the minimum bound of 0.38 s from [9]. In the next scenario, the platoon uses the same time headway but packet losses are enabled using the Gilbert channel described earlier. This can be confirmed visually as well since the L_∞ norms are in the order: $\|e_1\|_\infty \geq \|e_3\|_\infty \geq \|e_5\|_\infty$. That is, the maximum spacing errors diminish across the platoon. Please note that the maxima for each curve is that over the entire simulation interval, as per the L_∞ definition of string stability. We can see from the second subplot in Fig. 4.1 that maintaining the same time headway induces string instability, since the last follower's maximum spacing error is larger than that of the first. Finally, since equation

(3.30) yields a minimum value of 0.53 s, the third platoon operates under the same lossy V2V channel but with the headway chosen as 0.6 s, resulting in a string stable platoon. A headway of 0.6 s is smaller than the minimum for an ACC platoon (0.8 s) and that for a lossy one-vehicle lookup platoon (0.73 s) [21], so there is no need to degrade the platooning mode.

4.2 Higher-Fidelity Model Development

Since we are concerned about longitudinal string stability, it is sufficient to capture the behavior of the drive-line and braking system of a vehicle, ignoring lateral dynamics. A variety of longitudinal models are available in literature depending on components of interest (engine/transmission/tires) and level of fidelity required [41–43]. Many of them either require extensive data collection or privileged information from the vehicle/component manufacturer. Open source simulators like SUMO [44] ignore the actuation lags characteristic of real vehicles and past researchers in this area have often used simplified linear models for their validation [13, 17]. Instead, we utilize an empirical vehicle model for validation, similar to [45] and develop throttle/brake maps that relate pedal inputs and vehicle speed to acceleration generated. These signals are typically available directly on the onboard CAN bus of any drive-by-wire capable vehicle. In our case, an AutonomouStuff instrumented 2017 Lincoln MKZ hybrid car was used. Unlike in [45], there was no need to model the transmission explicitly since the MKZ hybrid car uses a continuously variable transmission.

The throttle and brake maps are presented in Figs. 4.2 and 4.3. Data was collected by cycling through different combinations of pedal inputs and velocities. Supplemental points were added manually at the extremities of the brake map to saturate the deceleration estimates and for smoother interpolation. The surface fit was obtained using 'gridfit' function in MATLAB. These maps, and the vehicle model in Simulink are available in a Github repository [1].

To validate the model developed, a test run was performed on the real vehicle through manual driving. The throttle and brake inputs were recorded (as shown in Fig 4.4) and the same was supplied to the longitudinal model in simulation. The recorded acceleration and velocity of the

[1] https://github.com/VegaVK/CACC_TAMU

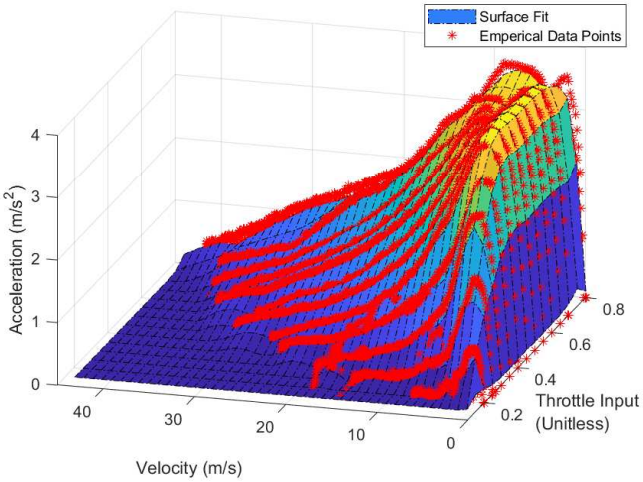

Figure 4.2: Throttle map of 2017 Lincoln MKZ generated from collected data. Reprinted with permission from [20]. ©2021 IEEE.

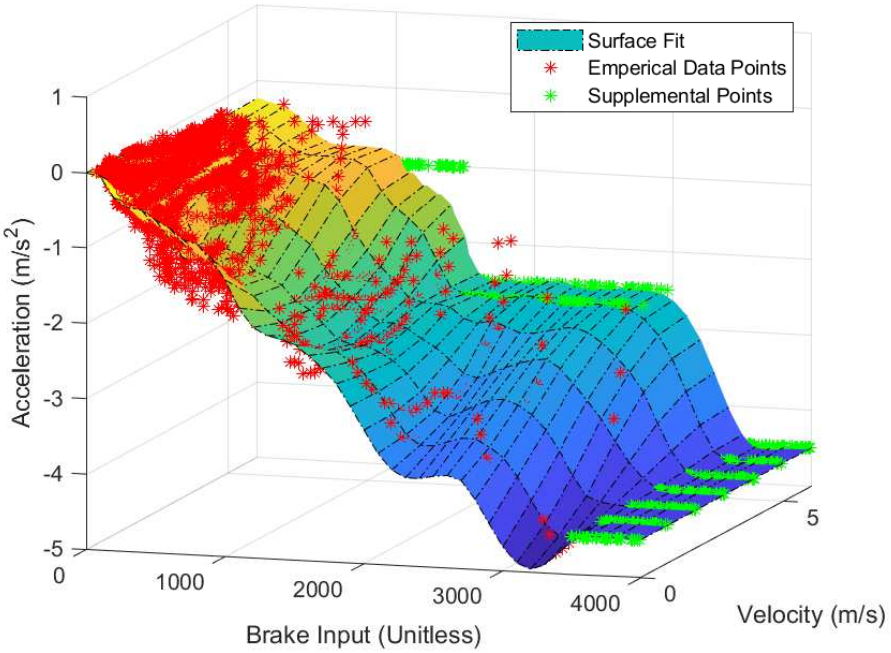

Figure 4.3: Brake map of 2017 Lincoln MKZ generated from collected data. Reprinted with permission from [20]. ©2021 IEEE.

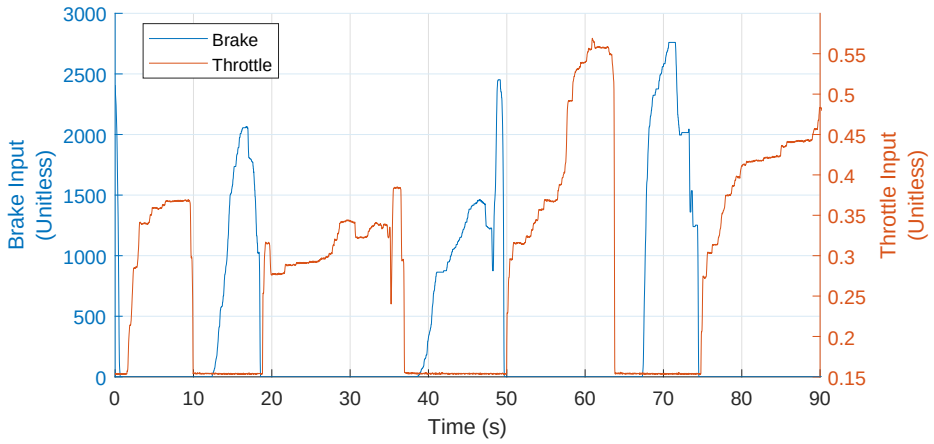

Figure 4.4: Brake and throttle inputs used for validation. Reprinted with permission from [20]. ©2021 IEEE.

real vehicle is compared with the output of the simulated vehicle in Fig. 4.5.

As we can see, the developed model is able to capture the longitudinal dynamics of the real vehicle and predict the variables of interest (acceleration and velocity) with sufficient fidelity. Position of the vehicle is obtained through integration and is not as important for model validation as the platoon controllers only require relative position while they require absolute velocity and absolute acceleration. Next, we will use this newly validated model to corroborate the lossy CACC and CACC+ control schemes for a variety of time headway settings.

4.3 CACC/CACC+ Simulations with Validated Car Model

We use the same Gilbert burst channel parameters and the same lead vehicle maneuvers as in Section 4.1. For lossy one vehicle lookup (CACC), the following controller gains were used: $(K_a, K_v, K_p) = (0.8, 1.5, 2)$. Actuation braking lag in the Lincoln MKZ was measured to be 0.37 s, based on the deceleration step response on the real vehicle. This value was used for τ to calculate the minimum time headway. Three scenarios are presented in Fig. 4.6 with a platoon of validated virtual vehicles: first without any losses and a time headway of 0.45 s, then with losses enforced in the V2V link, and finally after increasing the time headway to 0.6 s.

For lossy one-vehicle lookup, the sufficient minimum condition for headway, from equation

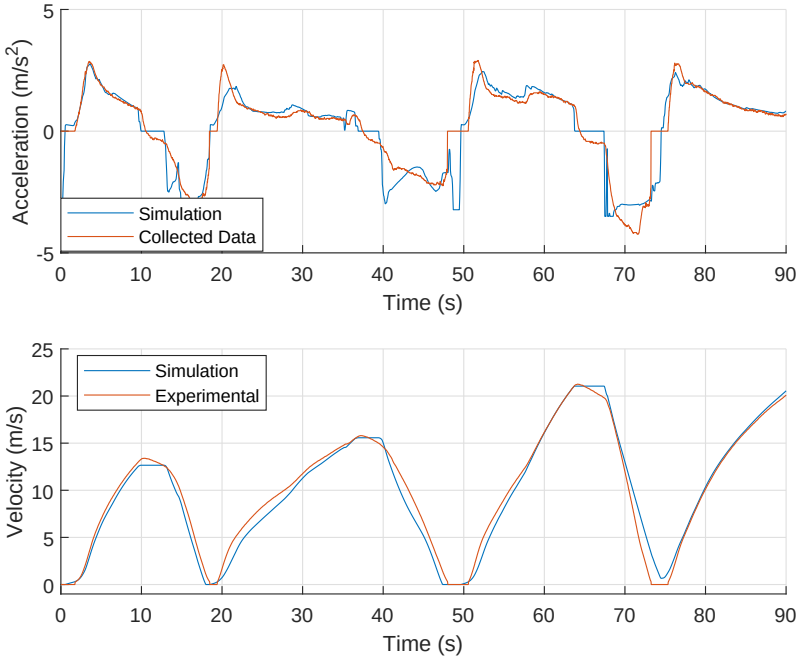

Figure 4.5: Model validation of longitudinal acceleration and velocity. Reprinted with permission from [20]. ©2021 IEEE.

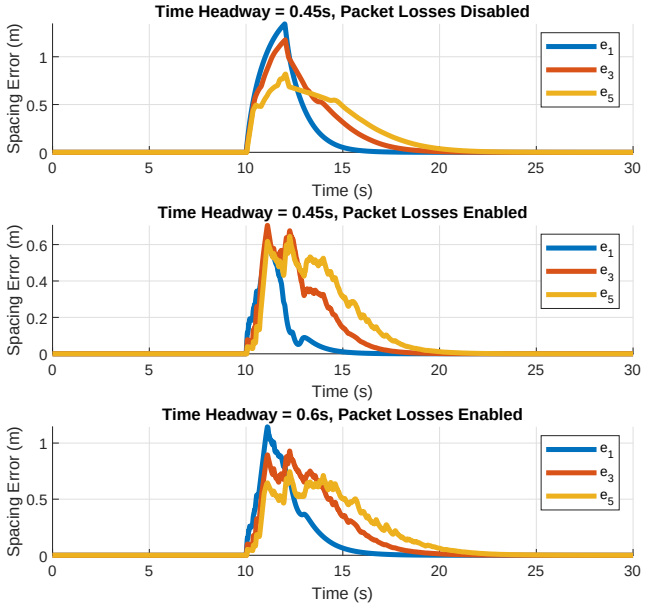

Figure 4.6: Spacing errors a CACC platoon with high fidelity model under different scenarios. Reprinted with permission from [20]. ©2021 IEEE.

(3.16), is 0.538 s. So as expected, an adjusted headway of 0.6 s provides string stability with the spacing errors diminishing across the platoon, while a headway of 0.45 s is unstable if the communication link is not ideal. There is no need to degrade the platoon to ACC mode (for which the sufficient condition on the minimum time headway is $2\tau = 0.74$ s).

Remark: If we compare the first two subplots in Figure 4.6, we will see that the magnitude of the spacing errors when packets are dropped (second subplot) are less than in the first where the communication channel is ideal. This may seem counter-intuitive at first. Let us consider the first following vehicle. In the control law in the lossy CACC case from eq. (2.5), when the packet is dropped at some time t, $\hat{w}(t) = 0$, dropping the acceleration term a_{i-1}. Since we have considered the first following vehicle, whose immediately preceding vehicle is the platoon leader (a deterministic vehicle), $a_{i-1}(t)$ for both the lossless and lossy scenarios will be the same. Nevertheless, the relative velocities and spacing errors for the first follower need not be the same for both scenarios at every time t. Thus, one cannot consider the control output for the lossy scenario at any time t to simply be the same as that for the ideal communication scenario with the acceleration term missing. Figure 4.7 shows the comparison of the acceleration of the same vehicle (first follower) in the first and second scenarios. We can see that the deceleration in the lossy scenario is, on average, larger than that of the ideal communication case. This aggressive deceleration causes the magnitude of the spacing errors for the first follower to be smaller in the second scenario. Nevertheless, because the string is unstable in the second scenario, the spacing errors may blow up and eventually exceed that of the first for a sufficiently large platoon.

Similarly, three scenarios for a two vehicle (CACC+) scheme are presented in Fig. 4.8. The gains used were: $(K_a, K_v, K_p) = (0.75, 2.5, 1.5)$. Again, we observe that a time headway that would otherwise be stable under ideal V2V communication becomes unstable when packet losses are introduced. The minimum headway for the given value of γ from equation (3.30) is 0.371 s so picking a headway of 0.4 s stabilizes the platoon, without the need to degrade to a CACC scheme.

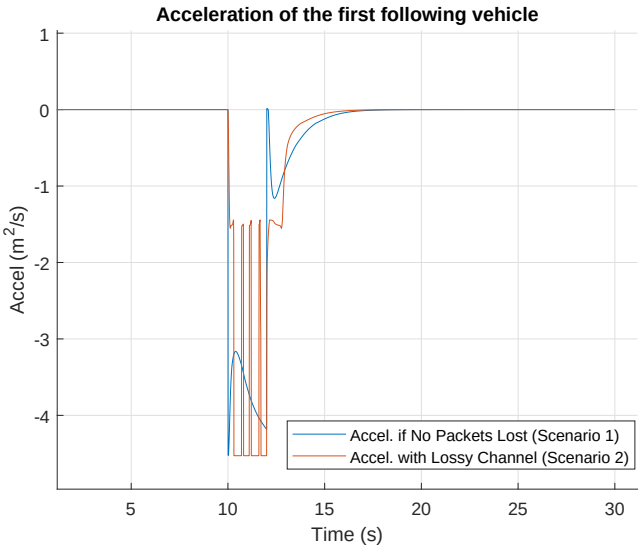

Figure 4.7: Comparison of Accelerations of the first follower vehicle in the first two scenarios

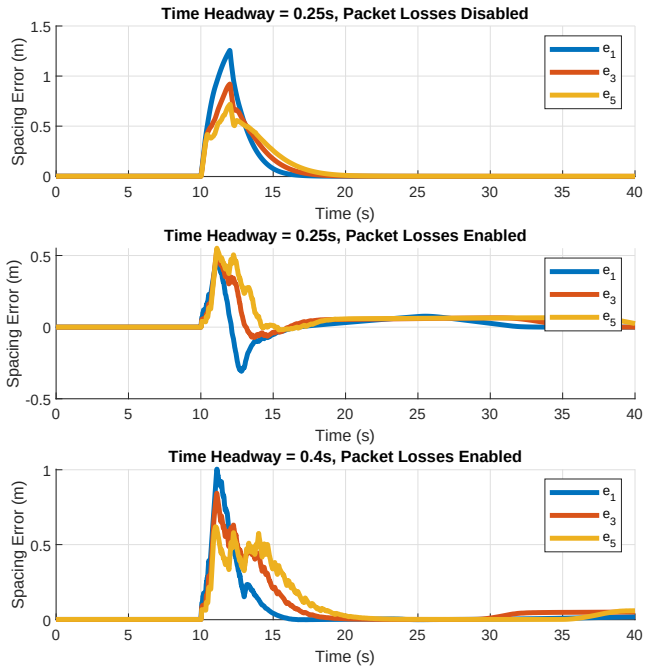

Figure 4.8: Spacing errors a CACC+ platoon with high fidelity model under different scenarios. Reprinted with permission from [20]. ©2021 IEEE.

4.4 Tests with Virtual Vehicle

We can go one step further for corroborating the derived sufficient conditions on time headway by performing real tests with a single vehicle.

The testing methodology is as follows. The vehicle is first manually driven and its GPS position, velocity and acceleration information is stored as a function of time with $t = 0$ at vehicle start. This is stored as the lead vehicle trajectory. Next, the vehicle is put in autonomous mode and the lead vehicle trajectory information is passed to it. With this information, the car now acts as the first follower vehicle and attempts to maintain a desired spacing to the (virtual) lead vehicle's trajectory in the previous run. The follower vehicle's trajectory is also stored as a time series and then passed to the car again as virtual sensor input to the second follower vehicle. In this way, the entire platoon can be run experimentally by running just one car at a time. Please note that each of the following vehicles' controllers do not see the entire trajectory of the virtual preceding vehicle. That is, they do not have information about the future actions (on the virtual time axis). Also, in order to simulate lossy wireless channel, a Gilbert noise model was implemented as a function to randomly drop the acceleration information (for CACC) that is sent to the controller. The details of the implementation can be perused on the GitHub repository for this work [2]. A list of the parameters of the vehicle controller and transition probabilities for the Gilbert Model used are shown in Table 4.1.

Table 4.1: List of Parameters used for Vehicle Controller and Wireless Channel

Parameter	**Value**
K_a	0.6
K_v	0.3
K_p	0.2
Good to Bad (P)	0.3
Bad to Good (Q)	0.3
Loss Ratio in Bad State (R)	0.95
Effective Reception Rate (γ)	0.525

[2] https://github.com/VegaVK/CACC_TAMU

A Piksi rover and base station combination was used to get Real-Time Kinematic (RTK) GPS data to measure the vehicle's position. The velocity was measured from the onboard CAN bus and an Inertial Measurement Unit (IMU) was used to measure acceleration. Figure 4.9 shows the velocity profile maintained by the manually driven lead vehicle. It starts from a stationary state to reach nearly 40 mph (18 m/s) and then suddenly decelerates to about 15 mph (7m/s) and then comes to a complete stop. We are interested in studying the error propagation behavior during the sudden deceleration.

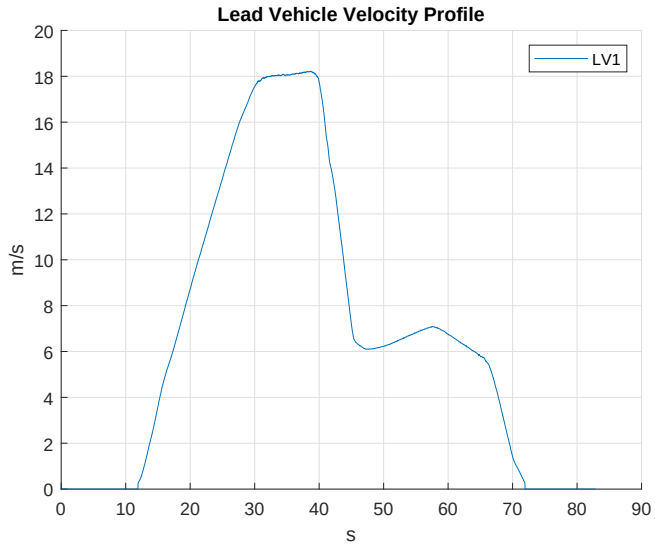

Figure 4.9: Velocity profile of the manually driven lead vehicle.

Similar to CACC simulations in Section 4.3, we first run a platoon with no packet losses (packet loss channel disabled). We know that the minimum string stable time headway for an ideal communication link is:

$$\frac{2\tau}{1+K_a} = 0.5s.$$

With the given $\gamma = 0.525$, we can now use our result to calculate the minimum sufficient time

headway for string stability with a lossy channel:

$$\frac{2\tau}{1+\gamma K_a} = 0.61s.$$

Indeed, we can observe from Figure 4.10 that when no packets are lost, a time headway of $h_w = 0.55s$ is sufficient for string stability since the peak of the spacing error of the fifth following vehicle is smaller than that of the first. Please note that even though the spacing errors increase at first for e_2 and e_3, they later diminish towards the tail end of the platoon. So, the platoon is still string stable.

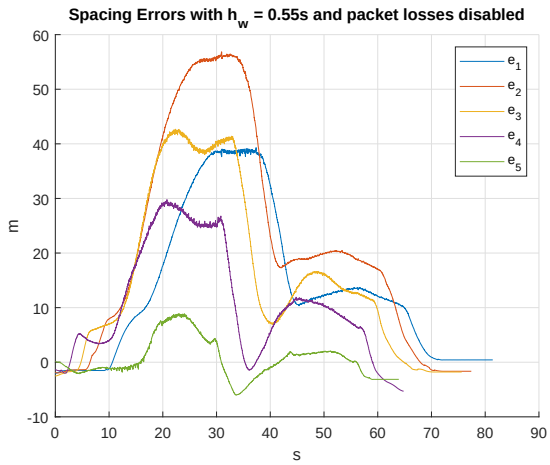

Figure 4.10: Spacing errors from experimental data with $h_w = 0.55s$ and no packet losses, showing that the platoon is string stable

When packet losses are present, the same time headway is insufficient and we see that the peak of the spacing errors start to magnify in Figure 4.11. Finally in Figure 4.12, we see that after readjusting the time headway to $0.65s$, we regain string stability.

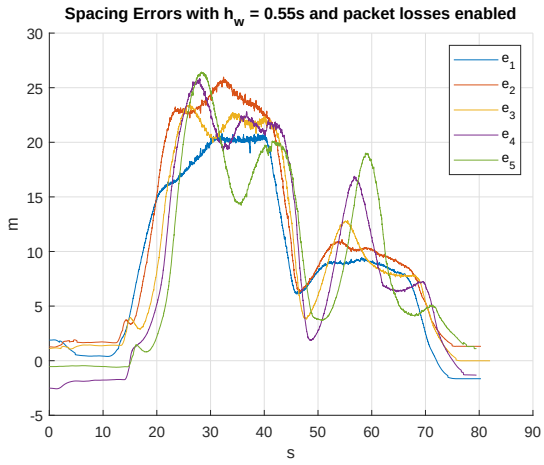

Figure 4.11: Spacing errors from experimental data with $h_w = 0.55s$ with packet losses, showing that the platoon is unstable

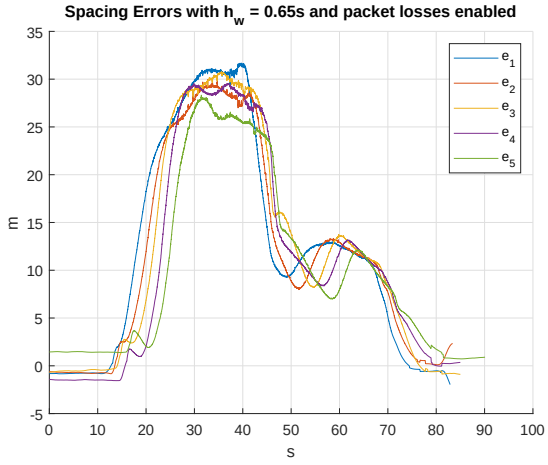

Figure 4.12: Spacing errors from experimental data with $h_w = 0.65s$ with packet losses, showing that the platoon has regained string stability

5. AVFS:UNIFORM BOUND ON SPACING ERRORS

As mentioned in Chapter 1, the string stability condition is usually expressed as a constraint on the error transfer function in the frequency domain. Suppose e_i and e_{i-1} are the spacing errors of two consecutive vehicles in the platoon. Then, in the Laplace domain, we can define

$$H(s) = \frac{E_i(s)}{E_{i-1}(s)}. \tag{5.1}$$

For platoon to be string stable, the constraint is that errors should diminish across the platoon. That is,

$$\|H(jw)\|_\infty \leq 1. \tag{5.2}$$

Strictly speaking, this is an approximation, since this condition only enforces the power of the spacing error signals (the 2-norm) to diminish, but not necessarily the maximum spacing error (the ∞-norm). In this chapter, we derive a property of string stable platoons that shows that the maximum spacing error in a platoon of any length can be uniformly upper bounded, as long as the lead vehicle's acceleration maneuvers are bounded in magnitude and time.

Let a platoon consist of $N+1$ vehicles, with the lead vehicle indexed starting from 0 and each of the automated follower vehicles indexed $i = 1, 2, \cdots N$. We will use $\mathcal{I}_N := \{1, 2, \ldots, N\}$ to represent the set of follower vehicles. Let the state of the i^{th} vehicle be denoted by $\zeta_i(t) \in \mathbb{R}^n$, while $y_i(t)$ represents its output (such as spacing errors or its derivatives with respect to some origin). Let the disturbance acting on the i^{th} vehicle be $d_i(t)$. We will use $\mathcal{S}_i$ to denote the set of vehicles whose information is available to the i^{th} vehicle for feedback. In applications such as Adaptive Cruise Control (ACC) and Cooperative Adaptive Cruise Control (CACC), the set of vehicles from which information is available is $\mathcal{S}_i = \{i-1\}$ for a single preceding vehicle lookup scheme. This scenario is explored in Theorem 2. Theorem 3 explores multiple vehicle lookup

schemes, where we could have $\mathcal{S}_i = \{i-1, i-2, \ldots, i-r\}$, where r depends on the connectivity. For some appropriate functions f_{ij} and h_i, the evolution of spacing errors may be described by a set of equations of the form:

$$\dot{\zeta}_i = \sum_{j \in S_i} f_{ij}(\zeta_i, \zeta_j, d_i), \quad e_i = h_i(\zeta_i), \quad i \in \mathcal{I}_N, \tag{5.3}$$

where e_i is the spacing error of the i^{th} vehicle. Please note that the time argument (t) has been dropped for brevity, unless required. The equilibrium solution for the above set of coupled evolution equations is $\zeta_i = 0,\ i \in \mathcal{I}_N$. A generalized definition of string stability due to Ploeg et al [46], Besselink and Knorn [47] is used here:

Definition (Scalable Weak Input-State Stability): The nonlinear system is said to be scalably input-output stable if there exist functions $\beta \in \mathcal{KL}$ and $\sigma \in \mathcal{K}$ and a number N_{min} such that for any $N \geq N_{min}$ and for any bounded disturbances $d_i(t),\ i \in \mathcal{I}_N$,

$$\max_{i \in \mathcal{I}_N} \|\zeta_i(t)\| \leq \beta(\sum_{i \in \mathcal{I}_N} \|\zeta_i(0)\|, t) + \sigma(\max_{i \in \mathcal{I}_N} \|d_i(t)\|_\infty).$$

The right hand side in the above equation is larger and generalized version of the bound presented in [47].

We will use the following definition for string stability [48]: Suppose a string of vehicles with one-predecessor lookup scheme can be modeled as a set of differential equations of the form:

$$\dot{x_i} = Ax_i + B\epsilon_{i-1}$$

$$\epsilon_i = Cx_i + D\epsilon_{i-1},$$

where $i = 1, 2, , \ldots$, and $x_i(t) \in \mathbb{R}^n$ forall i and t. Then, a string is considered L_∞ stable if given any $\gamma > 0$, there exists a $\delta > 0$ such that:

$$\sup_k \|x_k(0)\|_\infty < \delta \implies \sup_k \|x_k(t)\|_\infty < \gamma. \tag{5.4}$$

The frequency domain condition can then be obtained from this definition [48] as:

$$\|H_1(j\omega)\|_\infty \leq 1. \tag{5.5}$$

With feedback linearization, equation (5.3) reduces to the equations in Theorem 2 where $w_0(t)$ denotes the acceleration input of the lead vehicle, A_0 is Hurwitz matrix, B, C, D are respectively constant matrices.

For the platoon of homogeneous vehicles with one-predecessor lookup scheme, one obtains the following error evolution equations using a Laplace transformation [8, 9]:

$$Y_i(s) = H(s)Y_{i-1}(s),$$

where $H(s)$ is a rational, proper, stable transfer function. The requirement of string stability has thus far [8, 49, 50] been used as $\|H(jw)\|_\infty \leq 1$.

From [51], it is known that the input-output relationship for a rational, proper transfer function is:

$$\|y_i\|_2 \leq \|H(jw)\|_\infty \|y_{i-1}\|_2,$$

where the input and output are measured by their $\mathcal{L}_2$ norms (power in the error signals). Practical consideration for this application requires us to consider $\|y_i\|_\infty$ (the maximum value of the output) as it has direct bearing on safety. Accordingly, the corresponding input-output relationship from [51] is

$$\|y_i\|_\infty \leq \|h(t)\|_1 \|y_{i-1}\|_\infty,$$

where $h(t)$ is the unit impulse response of the transfer function $H(s)$. It is known from [51] that $H(0) \leq \|H(jw)\|_\infty \leq \|h(t)\|_1$ and that $H(0) = \int_0^\infty h(t) = \|h(t)\|_1$, when $h(t) \geq 0$ for all $t \geq 0$. Typical information flow structures such as the one for ACC and CACC are such that $H(0) = 1$, thereby putting a lower bound on $\|h(t)\|_1 = 1$. However, for ascertaining string stability, one must

attain this lower bound; an obstacle to attaining the lower bound is to find controller gains that render the unit impulse response of $H(s)$ non-negative. This is a variant of the open problem of transient control and there are currently no systematic procedures for determining the set of gains for this case.

In the first theorem, we exploit the bounded structure of leader's acceleration and finite duration of lead vehicle maneuvers to prove that it suffices to consider $\|H(jw)\|_\infty \leq 1$ to show the *uniform* boundedness of spacing errors. The first theorem is replicated from [22] for completeness and clarity.

Theorem 2. *Suppose:*

- *The error propagation equations are given by*

$$\dot{\zeta}_1(t) = A_0\zeta_1(t) + Dw_0(t), \tag{5.6}$$

$$\dot{\zeta}_i(t) = A_0\zeta_i(t) + By_{i-1}(t), \quad \forall i \geq 2 \tag{5.7}$$

$$y_i(t) = C\zeta_i(t), \quad \forall i \geq 1, \tag{5.8}$$

  and A_0 is a Hurwitz matrix;

- *the lead vehicle executes a bounded acceleration maneuver in finite time, i.e., $w_0(t) \in \mathcal{L}_2 \cap \mathcal{L}_\infty$;*

- *$\|C(jwI - A_0)^{-1}B\|_\infty \leq 1$ and*

- *For some $\alpha^* > 0$, $\sum_{i=1}^{N} \|\zeta_i(0)\| \leq \alpha^*$ for every N.That is, initially all spacing errors are absolutely summable.*

Then, there exists a $M_1, M_2 > 0$, independent of N, such that for all $i \geq 1$:

$$\|y_i(t)\|_\infty \leq M_1\alpha^* + M_2\|w_0(t)\|_2.$$

Proof. Since A_0 is Hurwitz, we can obtain the following using equations Linear System Theory [51] for some constants $\beta_2, \beta_\infty, \gamma_2, \gamma_\infty$:

$$\begin{aligned}
\zeta_1(t) &= e^{A_0 t}\zeta_1(0) + \int_0^t e^{A_0(t-\tau)} D w_0(\tau) d\tau, \\
\zeta_i(t) &= e^{A_0 t}\zeta_i(0) + \int_0^t e^{A_0(t-\tau)} B y_{i-1}(\tau) d\tau, \ i \geq 2, \\
\Rightarrow \|y_1(t)\|_2 &\leq \beta_2 \|\zeta_1(0)\| + \gamma_2 \|w_0(t)\|_2, \\
\|y_1(t)\|_\infty &\leq \beta_\infty \|\zeta_1(0)\| + \gamma_\infty \|w_0(t)\|_\infty, \\
\|y_i(t)\|_2 &\leq \beta_2 \|\zeta_i(0)\| + \|y_{i-1}(t)\|_2, \quad i \geq 2.
\end{aligned}$$

Note that the last inequality results from $\|C(jwI - A_0)^{-1}B\|_\infty \leq 1$. These inequalities can be combined as:

$$\begin{aligned}
\|y_i(t)\|_2 &\leq \beta_2 (\sum_{j=2}^{i} \|\zeta_j(0)\|) + \|y_1(t)\|_2, \\
&\leq \beta_2 (\sum_{i \in \mathcal{I}_N} \|\zeta_i(0)\|) + \gamma_2 \|w_0(t)\|_2, \\
&\leq \beta_2 \alpha^* + \gamma_2 \|w_0(t)\|_2.
\end{aligned}$$

Corless et al [52] have provided bounds on the L_∞ norm of the output, given an L_2 input for an asymptotically stable system. Using their approach, it follows that if we can optimize a scalar J:

$$\begin{aligned}
J := \min\{g\}, \quad &\text{subject to:} \\
C^T P C - gI \prec 0, g \in \mathbb{R}^+ \\
P \succ 0, \quad A_0 P + P A_0^T + B B^T = 0,
\end{aligned}$$

then for some $\eta > 0$ and for all $i \geq 1$,

$$\begin{aligned} \|y_i(t)\|_\infty &\leq \eta\|\zeta_i(0)\| + \sqrt{J}\|y_{i-1}(t)\|_2, \\ &\leq (\sqrt{J}\beta_2 + \eta)\alpha^* + \sqrt{J}\gamma_2\|w_0(t)\|_2. \end{aligned}$$

This completes the proof. □

Remark: If the platoon has a finite number of vehicles then the last condition on the sum of absolute initial errors can be trivially satisfied. Since longitudinal maneuvers of a vehicle change the speed of a vehicle from a constant to another constant in finite time, the lead vehicle's exogenous input $w_0(t)$ (e.g., its acceleration or jerk) can be assumed without any loss of generality to be square integrable.

Now, for a two vehicle lookup scheme, the requirement placed on the transfer functions is:

$$\|H_1(j\omega)\|_\infty + \|H_2(j\omega)\|_\infty \leq 1, \tag{5.9}$$

where:

$$\begin{aligned} \|H_1(s)\|_\infty &= \frac{Y_i(s)}{Y_{i-1}(s)} \\ \|H_2(s)\|_\infty &= \frac{Y_i(s)}{Y_{i-2}(s)} \end{aligned}$$

Consequently, we obtain an extension of Theorem 2 for a CACC+ policy:

Theorem 3. *Suppose the error propagation equations are given by*

$$\dot{\zeta}_1(t) = A_0\zeta_1(t) + Dw_0(t), \tag{5.10}$$

$$\dot{\zeta}_2(t) = A_0\zeta_2(t) + B_1y_1(t), \tag{5.11}$$

$$\forall i \geq 3, \quad \dot{\zeta}_i(t) = A_0\zeta_i(t) + B_1y_{i-1}(t) + B_2y_{i-2}(t), \tag{5.12}$$

$$\forall i \geq 1, \quad y_i(t) = C\zeta_i(t), \tag{5.13}$$

where A_0 is a Hurwitz matrix; furthermore, suppose that

- *the lead vehicle executes a bounded acceleration maneuver in finite time, i.e., $w_0(t) \in \mathcal{L}_2 \cap \mathcal{L}_\infty$;*
- $\|C(jwI - A_0)^{-1}B_1\|_\infty + \|C(jwI - A_0)^{-1}B_2\|_\infty \leq 1$ *and*
- *For some $\alpha^* > 0$, $\sum_{i=1}^{N} \|\zeta_i(0)\| \leq \alpha^*$ for every N.*

Then, there exists a $M_1, M_2 > 0$, independent of N, such that for all $i \geq 1$:

$$\|y_i(t)\|_\infty \leq M_1 + M_2\|w_0(t)\|_2.$$

Proof. For some constants $\beta_2, \beta_\infty, \gamma_2, \gamma_\infty$, we obtain:

$$\begin{aligned}
\zeta_1(t) &= e^{A_0t}\zeta_1(0) + \int_0^t e^{A_0(t-\tau)}Dw_0(\tau)d\tau, \\
\zeta_2(t) &= e^{A_0t}\zeta_2(0) + \int_0^t e^{A_0(t-\tau)}B_1y_1(\tau)d\tau, \\
\zeta_i(t) &= e^{A_0t}\zeta_i(0) + \int_0^t e^{A_0(t-\tau)}B_1y_{i-1}(\tau)d\tau \\
&\qquad + \int_0^t e^{A_0(t-\tau)}B_2y_{i-2}(\tau)d\tau, \ i \geq 2, \\
\Rightarrow \|y_1(t)\|_2 &\leq \beta_2\|\zeta_1(0)\| + \gamma_2\|w_0(t)\|_2, \\
\|y_1(t)\|_\infty &\leq \beta_\infty\|\zeta_1(0)\| + \gamma_\infty\|w_0(t)\|_\infty, \\
\|y_2(t)\|_2 &\leq \beta_2\|\zeta_2(0)\| + \|y_1(t)\|_2.
\end{aligned}$$

Using equation (5.9):

$$
\begin{aligned}
&\|y_i(t)\|_2 \\
&\leq \beta_2\|\zeta_i(0)\| + \|C(jwI - A_0)^{-1}B_1\|_\infty \|y_{i-1}(t)\|_2 \\
&\quad + \|C(jwI - A_0)^{-1}B_2\|_\infty \|y_{i-2}(t)\|_2 \\
&\leq \beta_2\|\zeta_i(0)\| \\
&\quad + \|C(jwI - A_0)^{-1}B_1\|_\infty \max\{\|y_{i-1}(t)\|_2, \|y_{i-2}(t)\|_2\} \\
&\qquad + \|C(jwI - A_0)^{-1}B_2\|_\infty \max\{\|y_{i-1}(t)\|_2, \|y_{i-2}(t)\|_2\} \\
&\leq \beta_2\|\zeta_i(0)\| + \max\{\|y_{i-1}(t)\|_2, \|y_{i-2}(t)\|_2\} \quad \forall i \geq 3.
\end{aligned}
$$

After simplification,

$$
\begin{aligned}
\|y_i(t)\|_2 &\leq \beta_2 \sum_{j=3}^{i} \|\zeta_i(0)\| + \max\{\|y_1(t)\|_2, \|y_2(t)\|_2\} \\
&\leq \beta_2 \sum_{j=1}^{i} \|\zeta_i(0)\| + \gamma_2\|w_0(t)\|_2
\end{aligned}
$$

From [52], it follows that if

$$
\begin{aligned}
J := \min\{g\}, \quad &\text{subject to:} \\
C^T P C - gI \prec 0, \\
P \succ 0, \quad A_0 P + P A_0^T + B_1 B_1^T + B_2 B_2^T = 0,
\end{aligned}
$$

then for some $\eta > 0$ and for all $i \geq 1$,

$$\begin{aligned}
\|y_i(t)\|_\infty &\leq \sqrt{J} \left\| \begin{matrix} y_{i-1} \\ y_{i-2} \end{matrix} \right\|_2 \\
&\leq \sqrt{J}(\|y_{i-1}(t)\|_2 + \|y_{i-2}(t)\|_2) \\
&\leq 2\sqrt{J}(\beta_2 \sum_{j=1}^{i} \|\zeta_i(0)\| + \gamma_2 \|w_0(t)\|_2) \\
&\leq M_1 + M_2 \|w_0(t)\|_2,
\end{aligned}$$

by setting $M_1 = 2\sqrt{J}\beta_2\alpha^*$ and $M_2 = 2\sqrt{J}\gamma_2$. This completes the proof. One requires $w_0(t) \in \mathcal{L}_\infty$ to guarantee that $\|y_i(t)\|_\infty$ is bounded. □

Remark: Theorem 3 can also be applied to a platoon with n-vehicle lookup scheme by modifying the string stability criterion to:

$$\sum_{k=1}^{n} \|H_k(j\omega)\|_\infty \leq 1$$

$$\text{i.e., } \sum_{k=1}^{n} \|C(jwI - A_0)^{-1} B_k\|_\infty \leq 1$$

This concludes the portion of this work on Automatic Vehicle Following Systems.

6. OBJECT TRACKING: SYSTEM SETUP

Now, we move the discussion to perception and object tracking for autonomous vehicles in difficult visibility conditions. A fully autonomous vehicle, as defined by the Society of Automotive Engineers, must be able to perform all driving functions (including perception) under all conditions. In order to achieve Level 5 autonomy, we need to design systems that work reliably even in adverse weather and visibility conditions, without the need for human intervention.

In this chapter, we describe a sensor stack consisting of a thermal camera system and radar that we are proposing to supplement regular cameras and lidars for tackling this challenge. We will also discuss some preliminary processing of the raw sensor data before the data association step, which will be covered in the next chapter.

6.1 Sensor Configuration and Data Acquisition

6.1.1 Hardware

Five (5) Automotive Development Kit 'ADK' thermal cameras were acquired from FLIR, with a field of view (FOV) of 50° each. For the radar, a 77 GHz Delphi ESR module was used, mounted to the front bumper of the car. For data collection, a 2017 Lincoln MKZ owned by the Mechanical Engineering Department at Texas A&M University was utilized as the driving platform. An Xsens IMU mounted in the trunk of the vehicle was used for collecting acceleration and orientation information. An RGB camera from PointGrey was also mounted to the inside windshield of the car, to serve as a reference. The data from the RGB camera was not used in the sensor fusion algorithm.

An intel NUC 8th Gen (NUC8i7HVK) with 4 cores and 32 GB RAM was used to interface all the sensors, including the vehicle's drive-by-wire system. All data was recorded on board and sensor fusion was done offline for convenience using an Nvidia RTX 2070 graphics card. Robot Operating System (ROS) was used as the primary middleware, with Ubuntu 18.04.

After multiple iterations through rapid prototyping (3D printing), a final design was created

such that the thermal camera system provided an output with a 190° total field of view. This was to demonstrate the ability of such systems to perceive a large portion of the scene, similar to a lidar. It is possible to develop a 360° FOV system with more cameras or different models of the ADK.

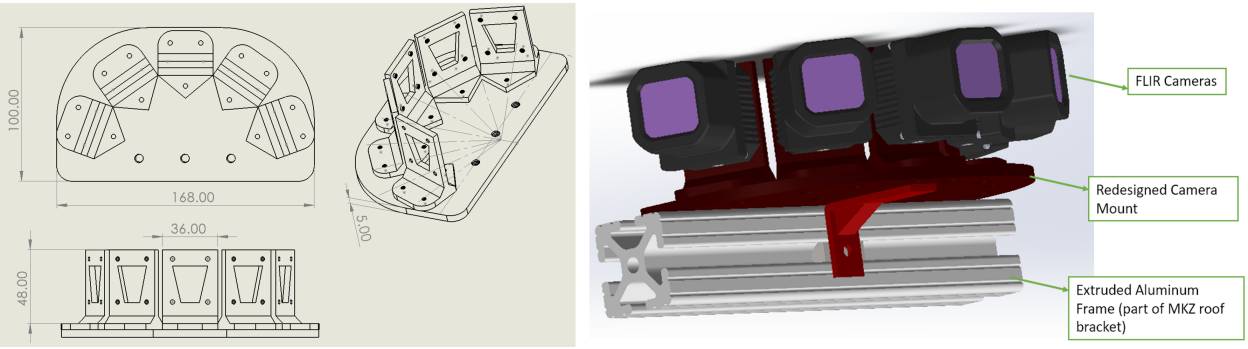

Figure 6.1: Final design of thermal camera system. All dimensions in millimeters

Figure 6.1 shows the key dimensions (in millimeters) of the designed mount, as well as a SolidWorks render. This design was machined in Aluminum and mounted to the vehicle rooftop. Figure 6.2 shows the thermal system after machining and assembly as well as the mounting location on the car.

Figure 6.2: Machined product and mounting location.

The measured relative distance between the camera and radar is shown in Figure 6.3. These dis-

tances were used for translating radar sensor measurements into the camera coordinate frame. The camera and radar were along the same geometric center line of the vehicle, facing the longitudinal direction of the car.

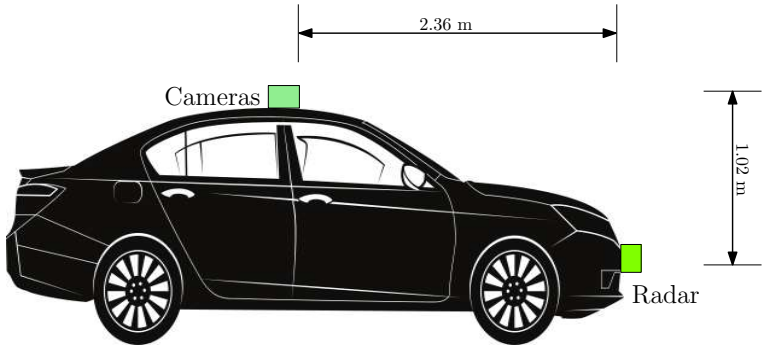

Figure 6.3: Relative position of the thermal cameras and radar.Reprinted with permission from [29]. ©SAE International.

In addition to these thermal cameras, a regular RGB camera was also mounted to the dashboard inside the vehicle, to serve as a reference for visual spectrum imaging. The data from this camera was not used as input to the object detection or tracking algorithms for this work. A GPS/IMU module from Xsens was used to obtain vehicle acceleration and heading necessary for sensor fusion, while the vehicle speed was recorded from the onboard CAN bus. All data streams were recorded at a minimum of 20 Hz sampling rate using ROS [53], an open source framework.

Since the relative angle between the optical axes of the cameras are fixed (and known), a script was written to stitch the video feeds from all the cameras to create a panoramic video. For this purpose, OpenCV tools were used to transform all cameras 1 through 5 to the image frame of the center camera (camera #3 in Figure 6.2). Then, overlapping portions of the images were cropped out to create a complete 190°FOV panorama. A screenshot of the stitched video is shown in Figure 6.4, showing a portion of the dataset collected on University Drive in College Station, TX. ROS device drivers for the FLIR ADK were supplied by the manufacturer but were designed for use with only one camera at a time. Consequently, the driver package was modified

to accommodate simultaneously collecting video streams from multiple cameras. The video is collected at 20 frames per second. The ROS package that was developed has been made available on GitHub [1].

Figure 6.4: A screenshot of a stitched video feed from the thermal cameras

Currently, each of the five thermal cameras perform their own Automatic Gain Control (AGC) as set by the manufacturer. This causes the 'banding' effect as seen in Figure 6.4. These bands did not adversely affect object detection performance, so no further action was taken.

6.1.2 Object Detection using YOLOv3

We used a well known state-of-the-art convolutional neural-network based object detector, YOLOv3 [54], to identify two classes of road users: car and people. The default trained weights for YOLOv3 were found to be unusable for identifying objects (especially cars) in the thermal spectrum. This is to be expected since the default network is trained on visible spectrum images. For the retraining task, we used an annotated thermal imaging dataset provided by FLIR [55] after making a few modifications to the configuration and retrained the network:

- The width and height parameters of the network were changed to 1280 and 256 respectively. This would enable better detection on the $5 : 1$ aspect ratio of the stitched video streams from the thermal camera assembly.

[1] https://github.com/VegaVK/flir_adk_multi

- Number of channels was changed to 3 from 1, since the LWIR cameras only output grayscale pixel information.
- Saturation and hue parameters were eliminated since these are only applicable for visible spectrum data.
- The data set provided by FLIR contains images of size 512×640 pixels, yielding a nearly $1:1$ aspect ratio. Each image in the dataset was padded on either side to generate a $5:1$ aspect ratio dataset. The size of the padding on each side was randomized while keeping the total padding width constant, so that the image from the FLIR dataset was not always at the center (as shown in Figure 6.5).

Figure 6.5: Random padding added to FLIR dataset images for training

The network was trained for 12,000 batches, after which it yielded satisfactory performance and was able to reliably detect cars and pedestrians both during day and at night. A sample screenshot of output of the YOLOv3 object detector is shown in Figure 6.6. The image was captured at night at a busy intersection and we can see that most of the vehicles are correctly identified with colored bounding boxes.

The position of the centers of these bounding boxes and their width/height are the considered as measurement outputs from the thermal camera system. Likewise, the mounted radar provides the relative longitudinal and lateral position of the radar returns, along with relative velocity of

Figure 6.6: Output of the object detector running on the thermal images

the object detected. These sensor measurements are then fused to create continuous tracks, as described in the next section.

7. OBJECT TRACKING: DATA ASSOCIATION

Once the sensor measurements are received, they need to be processed to remove false measurements ('clutter') and identify targets of interest. Once targets are established, they need to be tracked as it is important to have an estimate of the future trajectory of all road users for automated driving. For every new measurement received, a decision has to be made whether the measurement corresponds to any of the targets being tracked, if it necessitates the creation of a new track or if it should be discarded as clutter. This process of creating tracks from sensor measurements, updating the estimated trajectory of existing tracks with new measurements and destroying old tracks for objects that leave the region of interest is usually referred to as Data Association.

A variety of approaches for data association for multiple target tracking have been published in literature dating back to the late 1970s [56–58]. Many of the conventional approaches can be broadly separated into two classes: Single-Frame vs Multi-Frame data association, depending on whether the measurement-to-track association is made on a frame-by-frame basis, or if a history of 'likely assignments' are stored for a complete decision to be made later [59]. The simplest of the single frame methods is the Nearest Neighbor association where the sensor measurement closest to the track is associated with it and the rest are discarded as clutter. An optimal version of this algorithm, referred to as Global Nearest Neighbor association, uses the Kuhn-Munkres/Hungarian algorithm [60]. Alternatively, Joint Probabilistic Data Association (JPDA) first proposed by [61], uses a Bayesian approach to data association, effectively utilizing a weighted sum of all measurements in the neighborhood of a track. Multiple Hypothesis tracking is an example of the multi-frame association [62], and newer approaches also exist based on Random Set theory [63] and Particle Hypothesis Density [64]. A review of data fusion strategies is also available in [63]. In this work, we have adopted the use of single frame data association.

7.1 Methodology: Data Association for Multiple Object Tracking

Since the thermal camera and radar sensors provide different types of information, a direct application of any of the data association algorithms discussed would not be feasible. While extensions of JPDA to accommodate multi-modal sensors are available [65, 66] we employ a low cost, heuristic approach to the problem. We maintain separate trackers each for the thermal and radar data and then create a combined list of target tracks based on the confidence values from the YOLOv3 object detector. While this process of maintaining separate trackers for each of the two modalities imposes additional computational burden, we are able to obtain near-real time performance. The details of the camera and radar trackers are described below.

7.1.1 Model Assumptions

For thermal imaging, since the YOLOv3 algorithm yields bounding boxes, we chose to implement a modified version of a widely used, open source, real-time object tracker, SORT from [67]. The SORT algorithm assumes that the aspect ratio of the bounding boxes do not change. This would be true if the vehicles being tracked always remain within a certain angular range, but given that our thermal imaging system has an extremely wide-angle FOV of 190 degrees, objects often move from the front of the ego vehicle to the side while still being visible in the camera frame. This drastically changes the aspect ratio of the bounding boxes. So, we use a modified state vector while using a Kalman Filter to estimate and correct the state:

$$\vec{X} = [P_y, P_z, \dot{P}_y, \dot{P}_z, W, H, \dot{W}, \dot{H}]^T, \tag{7.1}$$

where P_y, P_z represent the coordinates of the center of each bounding box in the camera coordinate frame with $\dot{P}_y, \dot{P}_z$ as their derivatives. The longitudinal direction of travel of the vehicle was selected as the $+x$ direction, with the $+z$ direction pointing upwards from the surface of the road. $W, H, \dot{W}, \dot{H}$ denote the width and height of the bounding boxes, along with their derivatives. As mentioned earlier, only the center and dimensions of the bounding boxes are measurable from the thermal imaging system while their derivatives are not.

For the radar, the state vector is:

$$\vec{X} = [x, y, V_c, \beta]^T, \tag{7.2}$$

where x, y are the relative positions of the object being tracked with respect to the ego vehicle frame, V_c is its velocity and β is its heading angle. Only the first three states are directly measurable using the radar sensor. We implement an extended Kalman Filter from our research group's previous work on truck platooning [68].

We should note that for this work, we have assumed that each target (car/pedestrian) generates only one measurement and that no two targets can generate the same measurement. That is, a one-to-one mapping between the sensor readings and targets is assumed. This is not strictly true for the radar sensor; a single car can sometimes generate duplicate radar readings and extensions of the JPDA algorithm exist in published literature [69] that offer a modified formulation for such use cases.

7.1.2 Track Initiation

For track initiation, we compare data from two consecutive frames for each sensor. If any measurement in the second frame falls within a small neighborhood (5 pixels for the camera and 30 cm for the radar) of a measurement in the first frame, then we initiate a track. These bounds on the neighborhoods are reasonable since the sensors collect data at 20 Hz, with only 50 milliseconds between two consecutive measurement frames. Three-frame track initiation and Markov chain based initiators are also available in literature [66], but we were able to achieve reasonable performance with this method for our application.

7.1.3 Validation Gates and Track Maintenance

Once a set of tracks have been initiated, the camera and radar trackers group the incoming sensor measurements into clusters. This is done using ellipsoidal validation regions which are picked so as to maximize the probability that the true measurement from the track is within this region while minimizing the volume of the region. If two tracks are spatially close together, their

validation gates may overlap, as shown in Figure 7.1. In the figure, $\hat{T}^1$ and $\hat{T}^2$ are current targets and M_i, for $i = 1, 2, \ldots, 5$ are newly received sensor measurements. We can see that in this example, M_5 lies in the validation regions of both the targets of interest, so $\hat{T}^1$ and $\hat{T}^2$ would be clustered together.

A sensor measurement at time k is said to be within the validation region for a target, if the Mahalanobis distance between the predicted target position and the measurement is less then some threshold value as represented in the following equation:

$$[y_k - \hat{y}_{k|k-1}]^T S_k^{-1} [y_k - \hat{y}_{k|k-1}] \leq g^2, \tag{7.3}$$

where y_k is the sensor measurement at time k, $\hat{y}_{k|k-1}$ is the predicted target position obtained from the Kalman state estimator based on information up to time $k-1$, and S_k is the covariance of the innovation term in a standard Kalman filter formulation [59]. A scaling factor g is used to tune the volume of the ellipsoid.

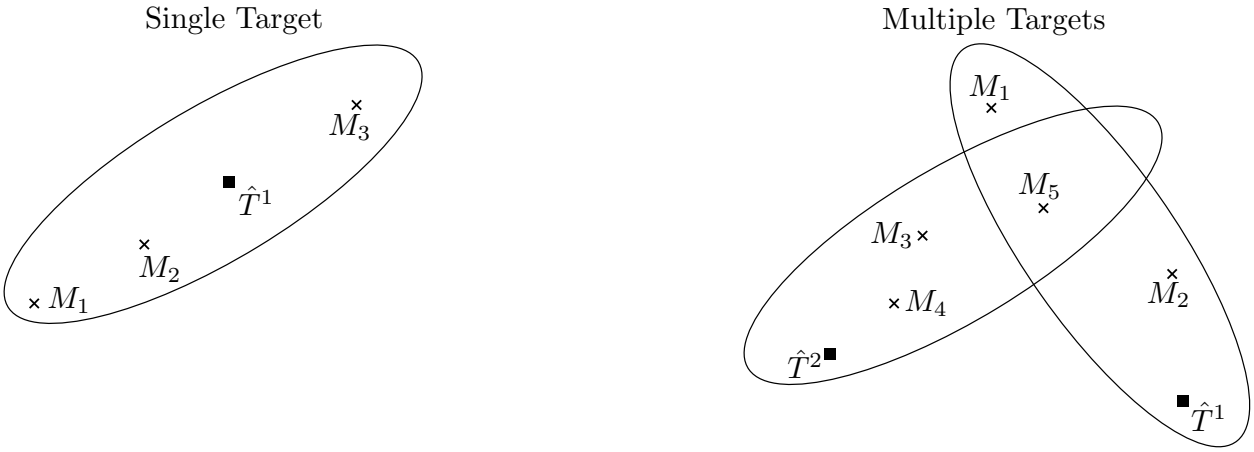

Figure 7.1: Validation regions for single and multiple target clusters.

Such clusters are created independently for the thermal imaging system and the radar. For thermal measurements, we implemented a greedy nearest neighbor association algorithm wherein

the closest measurement to a target within the validation region is assigned as the next measurement for that target. The FLIR cameras used are set to capture 20 frames per second. Given this frame rate and the ability of the trained YOLO network to offer consistent detection frame to frame, there was no need for advanced data association algorithms.

The radar measurements, on the other hand, were observed to contain a large amount of 'clutter'. For example, the radar often picks up trees on the sidewalk, the kerb of the sidewalk or any uneven portions of the road as obstacles due to its positioning close to the surface of the road. Given the low resolution of the radar, it does not offer any distinction between such clutter and targets of interest so we rely on the JPDA algorithm to generate tracks.

The JPDA algorithm requires the generation of all possible 'feasibility' event matrices [66] which is a combinatorial problem. For example, in the multiple target scenario presented in Figure 7.1 with two targets and five measurements, the total number of feasibility matrices is 31 [see Table 1 in [70]]. Generating these event matrices and calculating conditional probabilities for each can be time consuming especially if there are a large number of measurements associated with each cluster. To overcome this, [71] proposed a formulation that circumvents the need to generate event matrices, provided the the density of number of targets per cluster is low. In our dataset, we observed that a majority of clusters have three or less targets per cluster so the faster JPDA algorithm from [71] was implemented.

7.1.4 Track Destruction

When objects permanently move outside the field of view of the radar and imaging systems, their corresponding tracks need to be destroyed for computational efficiency. We achieve this by maintaining a time-to-death counter for each tracked object. The counter is dropped by 1 for every time step when none of the new measurements could be associated with an existing track and is reset if a measurement is successfully assigned to that track in the future. If the counter drops below a threshold, the track is deleted.

7.1.5 Combining Radar and Thermal Imaging Tracks

Finally, the radar and camera tracks are combined. All radar data is projected onto the camera plane through rigid transformations. If any of the object tracks identified lie within the bounding box of a track from the imaging system, then the position, velocity and heading is associated with that bounding box. Moreover, we observed that the thermal imaging system often provides more reliable tracks than the radar. We utilize the confidence score given by the YOLO object detector to identify cars/pedestrians that may not have been picked up by the radar due to occlusions or noise and elevate these as final tracks, even if no corresponding radar measurement is registered.

8. OBJECT TRACKING: VALIDATION OF RESULTS

Over 200 GB of data was collected in and around College Station, TX in a variety of conditions such as evening glare, night time and rain. A video link showing the tracking performance for the JPDA algorithm over a portion of the data set is available for viewing online [1].

While we have an implementation of the data association approach, it is difficult to evaluate its performance based solely on visual representation of the sensor fusion algorithms. Definitive object tracking metrics are available in literature [25], but these require the ground truth trajectories of all objects in the environment. We pursued a two-pronged approach to solve this issue. First, we validate the algorithm using simulated data where the ground truth is known. Then, we use a high resolution lidar (Ouster OS1-128) and manual annotations to experimentally validate the algorithm.

8.1 Validation Through Simulations

By creating a detailed urban environment with objects of interest, we can obtain the exact location and pose information of all objects in the scene. Then by running our data association algorithms in this virtual environment, we can compare the predicted tracks with the known trajectories to evaluate performance. MATLAB's automated driving toolbox was selected as it allowed simulation of cameras and radars as well as integration with Unreal Engine, for better visualization. A summary of the simulation setup is provided below.

Similar to the panoramic camera system mounted to the real vehicle, a set of 5 cameras was implemented using the 'Simulation 3D Camera' block in MATLAB. Output from each of these cameras is published as a ROS topic with the same characteristics as that of the real thermal cameras (resolution, frame rate, field of view etc). Consequently, we can generate a complete panorama in a similar manner as the experimental data. An example of the stitched panorama from the simulated camera sensors in a virtual environment is shown below.

[1] https://youtu.be/XvuI7pmFKpg

Figure 8.1: A screenshot showing stitched video, as seen through simulated cameras, from the ego vehicle.

Since the characteristics of the Delphi ESR radar have been experimentally measured by other researchers [72], we can readily use this information for tuning the parameters of the "Simulation 3D Probabilistic Radar" block in MATLAB to simulate the forward-facing radar. Again, the simulation is set up to publish ROS topics in the same format as that of the real radar on the car.

A custom traffic scenario was designed using the 'Driving Scenario Designer' tool in MATLAB. It involves two vehicles in front of the ego vehicle as well as two vehicles traveling in the opposite direction. Non-ego vehicles are set to perform lane change maneuvers so that we can test the performance of the sensor fusion algorithms in tracking vehicles that cross each other as well as those that are occluded. A video of the raw driving scenario designed is available to view online [2].

The final step for validation through simulation is to calculate the object tracking score. Since we know the exact (ground truth) positions of the simulated vehicles in the scene, we were then able to compare this with the output from the fusion algorithms. The output is given in the camera coordinates. The output of the sensor fusion algorithm and the ground truth can be written into file where each line is in the following format:

$$< frameID > \quad < TrackID > \quad < X > \quad < Y > \quad < Width > \quad < Height >$$

This encapsulates the X-Y coordinates of each bounding box in the camera frame (in pixels) as well

[2] https://youtu.be/-Bpy6wY6jgY

their width and height. In this way, the validation is done frame-by-frame. In each frame, both the number of objects detected and their position accuracy is validated. In order to standardize this validation, we are using an open-source library (py-motmetrics)[3] that calculates an MOT (Multiple Object Tracking) score from [73]. The output scores for virtual validation are presented in Table 8.1.

Table 8.1: MOT metrics for JPDA from Simulated Ground Truth.

Identification Precision (IDP)	**Identification Recall (IDR)**	**MOT Accuracy**	**MOT Precision**
44.7%	38.2%	46%	0.309

8.2 Validation Using Lidar

For experimental validation of our developed tracking systems, we have collected datasets with both lidar and thermal camera system. The Ouster OS1-128 lidar was also mounted on the roof of the vehicle, 15 cm vertically below the thermal camera assembly. This distance was small enough to assume that the camera and lidar had the same origin. Ground plane was segmented out from the lidar data and removed. Using the remaining lidar points, vehicles of interest were manually annotated using an open-source package [4]. A screenshot showing the annotations after ground plane removal is shown in Figure 8.2.

As is the simulated validation, a text file was generated using the annotated data as the ground truth and compared with the output of the sensor fusion algorithm. The MOT scores are presented in Table 8.2.

We observed that the scores were significantly lower for the experimental validation using lidar. There are two possible reasons for this. First is the quality of the annotations themselves. Since the precision score is decided at a pixel level, the positioning of bounding boxes in the

[3]https://github.com/cheind/py-motmetrics
[4]https://github.com/Earthwings/annotate

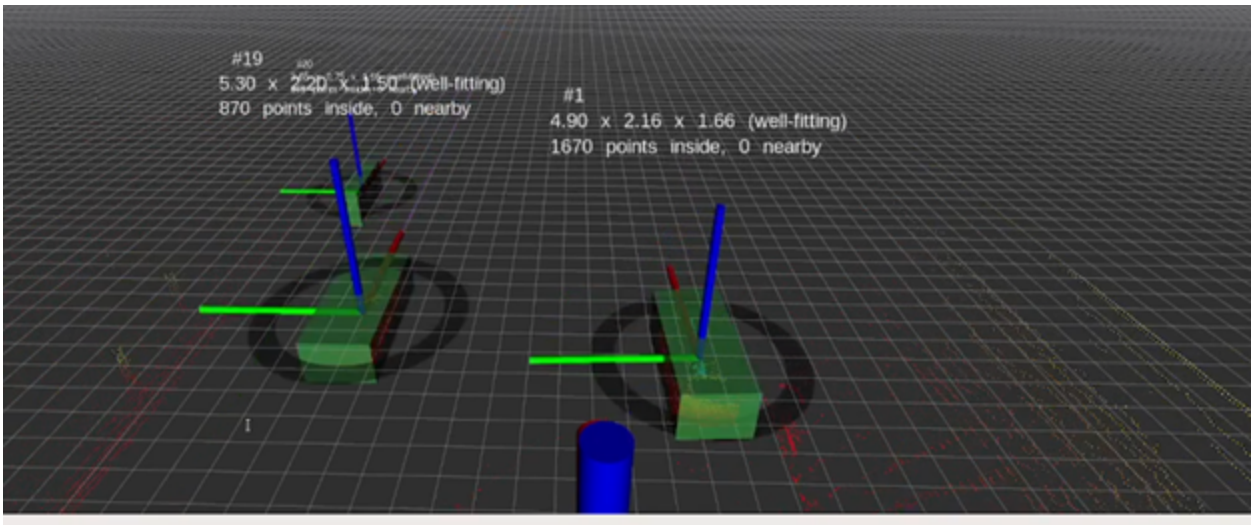

Figure 8.2: A screenshot showing manual lidar annotations after removal of ground plane.

Table 8.2: MOT metrics for JPDA from Lidar-based Ground Truth

Identification Precision (IDP)	**Identification Recall (IDR)**	**MOT Accuracy**	**MOT Precision**
24.6%	22.2%	15%	0.411

annotations significantly affects the result. In our case, the annotations were semi-automatically generated. The annotation process consisted of manually drawing bounding boxes for key frames and interpolating between these frames. The score can be improved by fine-tuning the annotations, which is a labor-intensive task.

Second, the lidar sensor's range is only up to 120m, but the thermal camera system was able to detect vehicles further away for which no lidar points existed in the point cloud. An example of this is shown in Figure 8.3. This resulted in the lower recall score. Nevertheless, this reinforces the superiority of the thermal perception system.

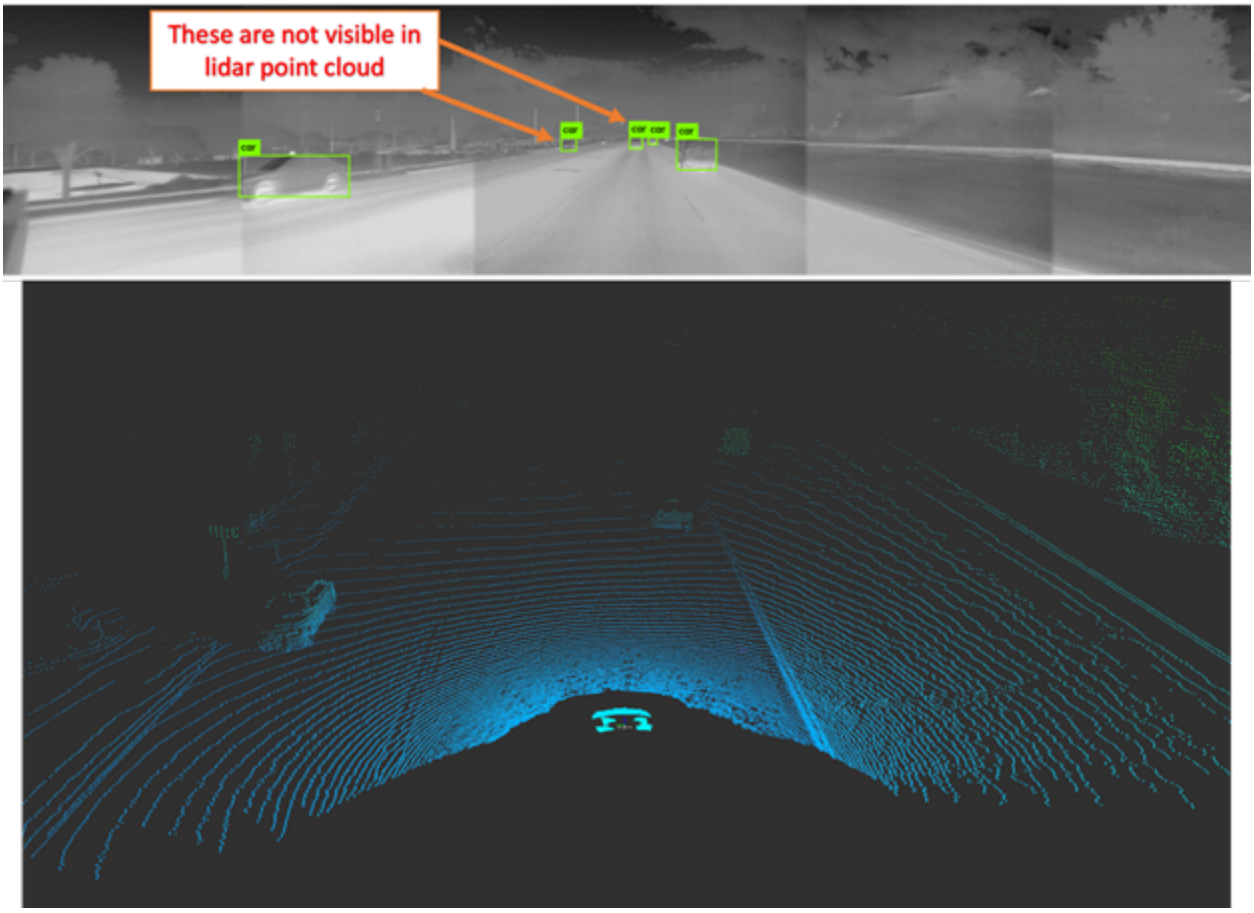

Figure 8.3: Example of cars that are far away, which are detectable by the thermal camera system but not by the lidar.

9. SUMMARY AND FUTURE WORK

Finally, in this chapter we present a brief summary of the two parts of the dissertation and discuss some recommended future avenues of research.

9.1 Automatic Vehicle Following Systems

From a fuel-efficiency and traffic congestion standpoint, it is important that platoons are able to achieve the smallest inter-vehicular gap while maintaining safety. In non-ideal environments vehicle platoons can become unstable due to packet drops. In the first few chapters of this work, we developed a real-time algorithm to adjust the time headway based on the packet reception rate. We demonstrated using high fidelity simulations as well as experimental runs with a passenger car, that these form a set of sufficient conditions to regain string stability when packet drops occur over the wireless link.

Then, we reexamined the notion of string stability from a practical perspective. The commonly used frequency domain condition for string stability is an approximation since it exerts a constraint on the power of the spacing error signal rather than its maximum amplitude. We proposed a method to uniformly bound spacing errors for any vehicle in a homgeneous platoon, given the platoon leader's motion. This may also serve as a guideline for selecting a safe stand-still distance.

For future work, it would be interesting to explore conditions for stability when not only the communicated information, but also the on-board information is lost. For example, in situations with a faulty radar sensor, the position and velocity information may not be available to the controller, requiring an adjustment to the time headway employed. Studying the effect of quantization in the feedback signal would also shed light on the precision of the sensors required for enabling platooning. Furthermore, we have ignored ride comfort in this study and focused on platoon stability. Ensuring a smooth ride by minimizing jerk while simultaneously guaranteeing string stability would also be of interest for a commercial implementation.

9.2 Object Tracking in Adverse Visibility

In the second part of this thesis, we tackle the perception problem for autonomous driving, with a focus on difficult visibility conditions. We demonstrate the benefits of using a thermal imaging system in combination with automotive radar to overcome this challenge.

First, a prototype hardware mount was designed and fabricated along with accompanying software that allows tracking of vehicles in a 190° FOV of the ego vehicle. After picking a suitable set of assumptions for the state estimator, we then utilized a probabilistic data association algorithm to fuse information from the thermal cameras and radars to successfully track vehicles in front of the ego vehicle in situations where an RGB camera would fail.

The results were validated using simulated data as well as using a state-of-the-art lidar sensor. It was observed that the combination of thermal and radar sensor can be used to supplement the existing perception stack. In fact, we observed that using thermal cameras we can extend the range of the perception system since vehicles can be detected in the thermal image even when they are beyond the detectable range of the lidar.

While we have mainly focused on direct glare from the sun and night-time driving, in the future, this part of the work can be improved by incorporating other weather phenomenon that contribute to poor visibility (such as heavy rain or snow). Additional side-facing radar sensors could potentially be used to improve the sensor fusion since the current radar only covers upto 120° FOV. In this way, the entire thermal panorama will have radar sensor coverage. Training the object detector for other classes of interest (trucks, bicycles, pets) and tuning separate trackers for these would also be a useful pursuit.

REFERENCES

[1] J. R. Treat, N. S. Tumbas, S. T. McDonald, D. Shinar, R. D. Hume, R. E. Mayer, R. L. Stansifer, and N. J. Castellan, *Tri-level study of the causes of traffic accidents: final report. Volume I: causal factor tabulations and assessments*. National Technical Information Service, 1977.

[2] NHTSA, *National Motor Vehicle Crash Causation Survey: Report to Congress: DOT HS 811 059*. Createspace Independent Pub, 2013.

[3] NHTSA-US Department of Transportation, "Automated driving systems: A vision for safety." `https://www.nhtsa.gov/sites/nhtsa.dot.gov/files/documents/13069a-ads2.0_090617_v9a_tag.pdf`, 2016.

[4] R. H. Robert E. Chandler and E. W. Montroll, "Traffic Dynamics: Studies in Car Following," *Operations Research*, 1958.

[5] J. Lioris, R. Pedarsani, and F. Y. Tascikaraoglu, "Platoons of connected vehicles can double throughput in urban roads," *Transportation Research Part C: Emerging Technologies*, vol. 77, pp. 292–305, 2017.

[6] A. Alam, B. Besselink, V. Turri, J. MåRtensson, and K. H. Johansson, "Heavy-duty vehicle platooning for sustainable freight transportation: A cooperative method to enhance safety and efficiency," *IEEE Control Systems Magazine*, vol. 35, no. 6, pp. 34–56, 2015.

[7] V. K. Vegamoor, S. Darbha, and K. R. Rajagopal, "A review of automatic vehicle following systems," *Journal of the Indian Institute of Science*, vol. 99, no. 4, pp. 567–587, 2019.

[8] S. Darbha, *String Stability Of Interconnected Systems: An Application To Platooning In Automated Highway Systems*. Phd dissertation, University of California Berkeley, 1994.

[9] S. Darbha, S. Konduri, and P. R. Pagilla, "Benefits of V2V communication for autonomous and connected vehicles," *IEEE Transactions on Intelligent Transportation Systems*, vol. 20,

no. 5, pp. 1954–1963, 2019.

[10] C. Lei, M. van Eenennaam, W. K. Wolterink, and J. Ploeg, "Impact of packet loss on cacc string stability performance," in *Proceedings of the 11th Intl. Conference on ITS Telecommunications*, 2011.

[11] F. J. Vargas, A. I. Maass, and A. A. Peters, "String stability for predecessor following platooning over lossy ommunication channels," in *23rd International Symposium on Mathematical Theory of Networks and Systems*, (Hong Kong), Hong Kong University of Science and Technology, 2018.

[12] J. Ploeg, E. Semsar-Kazerooni, G. Lijster, N. van de Wouw, and H. Nijmeijer, "Graceful degradation of cooperative adaptive cruise control," *IEEE Transactions on Intelligent Transportation Systems*, vol. 16, no. 1, pp. 488–497, 2015.

[13] F. Acciani, P. Frasca, A. Stoorvogel, E. Semsar-Kazerooni, and G. Heijenk, "Cooperative adaptive cruise control over unreliable networks: An observer-based approach to increase robustness to packet loss," *2018 European Control Conference, ECC 2018*, pp. 1399–1404, 2018.

[14] H. Xing, J. Ploeg, and H. Nijmeijer, "Padé approximation of delays in cooperative acc based on string stability requirements," *IEEE Transactions on Intelligent Vehicles*, vol. 1, no. 3, pp. 277–286, 2016.

[15] X. Liu, A. Goldsmith, S. S. Mahal, and J. K. Hedrick, "Effects of communication delay on string stability in vehicle platoons," in *ITSC 2001. 2001 IEEE Intelligent Transportation Systems. Proceedings (Cat. No. 01TH8585)*, pp. 625–630, IEEE, 2001.

[16] B. Besselink and K. H. Johansson, "String stability and a delay-based spacing policy for vehicle platoons subject to disturbances," *IEEE Transactions on Automatic Control*, vol. 62, pp. 4376–4391, 2017.

[17] T. Zeng, O. Semiari, W. Saad, and M. Bennis, "Joint communication and control for wireless autonomous vehicular platoon systems," *IEEE Transactions on Communications*, vol. 67, no. 11, pp. 7907–7922, 2019.

[18] 5GAA, "V2X functional and performance test report." Accessed: 4-1-2021.

[19] T. Kleinow, S. Lakshmanan, P. Richardson, V. Elangovan, S. Schmidt, J. Locke, and M. Crowder, "A validated model for non-line-of-sight V2X communications," in *2020 Antenna Measurement Techniques Association Symposium (AMTA)*, pp. 1–6, 2020.

[20] V. Vegamoor, S. Rathinam, and S. Darbha, "String stability of connected vehicle platoons under lossy v2v communication," *IEEE Transactions on Intelligent Transportation Systems*, pp. 1–12, 2021.

[21] V. Vegamoor, D. Kalathil, S. Rathinam, and S. Darbha, "Reducing time headway in homogeneous CACC vehicle platoons in the presence of packet drops," in *2019 18th European Control Conference (ECC)*, pp. 3159–3164, 2019.

[22] V. Vegamoor, S. Yan, S. Rathinam, and S. Darbha, "Mobility and safety benefits of connectivity in cacc vehicle strings," in *2020 IEEE 23rd International Conference on Intelligent Transportation Systems (ITSC)*, pp. 1–6, 2020.

[23] H. Gao, B. Cheng, J. Wang, K. Li, J. Zhao, and D. Li, "Object classification using cnn-based fusion of vision and lidar in autonomous vehicle environment," *IEEE Transactions on Industrial Informatics*, vol. 14, no. 9, pp. 4224–4231, 2018.

[24] D. Prokhorov, "A convolutional learning system for object classification in 3-d lidar data," *IEEE Transactions on Neural Networks*, vol. 21, no. 5, pp. 858–863, 2010.

[25] SAE, *Taxonomy and Definitions for Terms Related to On-Road Motor Vehicle Automated Driving Systems*, 2014.

[26] K. Poland, M. McKay, D. Bruce, and E. Becic, "Fatal crash between a car operating with automated control systems and a tractor-semitrailer truck," *Traffic Injury Prevention*, vol. 19, pp. S153–S156, 2018.

[27] N. Paul and C. Chung, "Application of hdr algorithms to solve direct sunlight problems when autonomous vehicles using machine vision systems are driving into sun," *Computers in Industry*, vol. 98, pp. 192 – 196, 2018.

[28] K. M. Judd, M. P. Thornton, and A. A. Richards, "Automotive sensing: assessing the impact of fog on LWIR, MWIR, SWIR, visible, and lidar performance," in *Infrared Technology and Applications XLV* (B. F. Andresen, G. F. Fulop, and C. M. Hanson, eds.), vol. 11002, pp. 322 – 334, International Society for Optics and Photonics, SPIE, 2019.

[29] A. S. Bhadoriya, V. K. Vegamoor, and S. Rathinam, "Object detection and tracking for autonomous vehicles in adverse weather conditions," in *SAE WCX Digital Summit*, SAE International, 2021.

[30] F. Bu, H. Tan, and J. Huang, "Design and field testing of a cooperative adaptive cruise control system," in *Proceedings of the 2010 American Control Conference*, pp. 4616–4621, 2010.

[31] R. Rajamani, S. B. Choi, B. K. Law, J. K. Hedrick, R. Prohaska, and P. Kretz, "Design and Experimental Implementation of Longitudinal Control for a Platoon of Automated Vehicles ," *Journal of Dynamic Systems, Measurement, and Control*, vol. 122, no. 3, pp. 470–476, 1998.

[32] E. N. Gilbert, "Capacity of a burst-noise channel," *Bell System Technical Journal*, vol. 39, no. 5, pp. 1253–1265, 1960.

[33] E. O. Elliott, "Estimates of error rates for codes on burst-noise channels," *The Bell System Technical Journal*, vol. 42, no. 5, pp. 1977–1997, 1963.

[34] H. A. Sanneck and G. Carle, "Framework model for packet loss metrics based on loss runlengths," in *Multimedia Computing and Networking 2000* (K. Nahrstedt and W. chi Feng, eds.), vol. 3969, pp. 177 – 187, International Society for Optics and Photonics, SPIE, 1999.

[35] K. Eshteiwi, B. Sleim, and G. Kaddoum, "Full duplex of v2v cooperative relaying over cascaded nakagami-m fading channels," in *2020 International Symposium on Networks, Computers and Communications (ISNCC)*, pp. 1–5, 2020.

[36] M. H. Rizvi and R. W. Shorrock, "A note on matrix-convexity," *The Canadian Journal of Statistics / La Revue Canadienne de Statistique*, vol. 7, no. 1, pp. 39–41, 1979.

[37] H. H. Nguyen, "Asymptotic lyapunov exponents for large random matrices," *Annals of Applied Probability*, vol. 27, no. 6, pp. 3672–3705, 2017.

[38] A. D. Jackson, B. Lautrup, P. Johansen, and M. Nielsen, "Products of random matrices," *Physical Review E - Statistical Physics, Plasmas, Fluids, and Related Interdisciplinary Topics*, vol. 66, no. 6, p. 5, 2002.

[39] S. Geman, "Some averaging and stability results for random differential equations," *SIAM Journal on Applied Mathematics*, vol. 36, no. 1, pp. 86–105, 1979.

[40] R. Khasminskii, *Stochastic Stability of Differential Equations*. Springer Science & Business Media, 2008.

[41] X.-Y. Lu and J. K. Hedrick, "Heavy-duty vehicle modelling and longitudinal control," *Vehicle System Dynamics*, vol. 43, no. 9, pp. 653–669, 2005.

[42] H. Pacejka, *Tire and vehicle dynamics*. Elsevier, 2005.

[43] R. N. Jazar, *Vehicle dynamics: theory and application*. Springer, 2017.

[44] M. Behrisch, L. Bieker-Walz, J. Erdmann, and D. Krajzewicz, "SUMO – simulation of urban mobility: An overview," in *Proceedings of SIMUL*, vol. 2011, 2011.

[45] V. K. Vegamoor, "Model based longitudinal control of heavy duty vehicles," 2018.

[46] J. Ploeg, N. van de Wouw, and H. Nijmeijer, "Lp string stability of cascaded systems: Application to vehicle platooning," *IEEE Transactions on Control Systems Technology*, vol. 22, pp. 786–793, March 2014.

[47] B. Besselink and S. Knorn, "Scalable input-to-state stability for performance analysis of large-scale networks," *IEEE Control Systems Letters*, vol. 2, pp. 507–512, July 2018.

[48] S. Darbha, "A Note About the Stability of a String of LTI Systems ," *Journal of Dynamic Systems, Measurement, and Control*, vol. 124, pp. 472–475, 07 2002.

[49] S. Sheikholeslam and C. A. Desoer, "Longitudinal control of a platoon of vehicles," in *1990 American Control Conference*, pp. 291–296, 1990.

[50] P. A. Ioannou and C. C. Chien, "Autonomous intelligent cruise control," *IEEE Transactions on Vehicular Technology*, vol. 42, no. 4, pp. 657–672, 1993.

[51] C. Desoer and M. Vidyasagar, *Feedback systems: input-output properties*. Electrical science series, Academic Press, 1975.

[52] M. Corless, G. Zhu, and R. Skelton, "Improved robustness bounds using covariance matrices," in *Proceedings of the 28th IEEE Conference on Decision and Control,*, pp. 2667–2672 vol.3, 1989.

[53] M. Quigley, B. Gerkey, K. Conley, J. Faust, T. Foote, J. Leibs, E. Berger, R. Wheeler, and A. Ng, "ROS: an open-source robot operating system," in *Proc. of the IEEE Intl. Conf. on Robotics and Automation (ICRA) Workshop on Open Source Robotics*, 2009.

[54] J. Redmon and A. Farhadi, "Yolov3: An incremental improvement," 2018.

[55] FLIR, "Thermal dataset for algorithm training," *FLIR Systems Inc.*, 2019.

[56] Y. Bar-Shalom and E. Tse, "Tracking in a Cluttered Environment With Probabilistic Data Association," *Automatica*, 1975.

[57] C. Morefield, "Application of 0-1 Integer Programming to Multitarget tracking problems," *IEEE Transactions on Automatic Control*, 1977.

[58] D. B. Reid, "An Algorithm for Tracking Multiple Targets," *IEEE Transactions on Automatic Control*, 1979.

[59] J. C. McMillan and S. S. Lim, "Data Association Algorithms for Multiple Target Tracking (U)," *Defense Research Establishment Ottawa*, 1990.

[60] J. Munkres, "Algorithms for the assignment and transportation problems," *Journal of the Society for Industrial and Applied Mathematics*, vol. 5, no. 1, pp. 32–38, 1957.

[61] T. E. Fortmann, M. Scheff, and Y. Bar-Shalom, "Multi-Target Tracking using Joint Probabilistic Data Association," 1980.

[62] S. Blackman, "Multiple Hypothesis Tracking For Multiple Target Tracking," *IEEE Aerospace and Electronic Systems Magazine*, 2004.

[63] J. Llinas, M. E. Liggins, and D. L. Hall, *Hand Book of Multisensor Data Fusion: Theory and Practice*. CRC Press, 2009.

[64] N. T. Pham, W. Huang, and S. H. Ong, "Probability hypothesis density approach for multi-camera multi-object tracking," in *Computer Vision – ACCV 2007* (Y. Yagi, S. B. Kang, I. S. Kweon, and H. Zha, eds.), (Berlin, Heidelberg), pp. 875–884, Springer Berlin Heidelberg, 2007.

[65] M. Munz, M. Mahlisch, and K. Dietmayer, "Generic Centralized Multi Sensor Data Fusion Based on Probabilistic Sensor and Environment Models for Driver Assistance Systems," *IEEE Intelligent Transportation Systems Magazine*, vol. 2, no. 1, pp. 6–17, 2010.

[66] Y. Bar-Shalom, *Multitarget-Multisensor Tracking Principles and Techniques*. YBS Publishing, 1995.

[67] A. Bewley, Z. Ge, L. Ott, F. Ramos, and B. Upcroft, "Simple online and realtime tracking," *2016 IEEE International Conference on Image Processing (ICIP)*, 2016.

[68] M. Liu, S. Rathinam, M. Lukuc, and S. Gopalswamy, "Fusing radar and vision data for cut-in vehicle identification in platooning applications," in *WCX SAE World Congress Experience*, SAE International, 2020.

[69] B. Habtemariam, R. Tharmarasa, T. Thayaparan, M. Mallick, and T. Kirubarajan, "A Multiple-Detection Joint Probabilistic Data Association Filter," *IEEE Journal of Selected Topics in Signal Processing*, vol. 7, no. 3, pp. 461–471, 2013.

[70] J. L. Fisher and D. P. Casasent, "Fast JPDA multitarget tracking algorithm," *Applied Optics*, vol. 28, no. 2, p. 371, 1989.

[71] B. Zhou and N. K. Bose, "Multitarget Tracking in Clutter: Fast Algorithms for Data Association," *IEEE Transactions on Aerospace and Electronic Systems*, vol. 29, no. 2, pp. 352–363, 1993.

[72] L. Stanislas and T. Peynot, "Characterisation of the delphi electronically scanning radar for robotics applications," in *Proceedings of the Australasian Conference on Robotics and Automation 2015* (H. Li and J. Kim, eds.), pp. 1–10, Australia: Australian Robotics and Automation Association, 2015.

[73] K. Bernardin and R. Stiefelhagen, "Evaluating Multiple Object Tracking Performance: The CLEAR MOT Metrics," *EURASIP Journal on Image and Video Processing*, vol. 2008, pp. 1–10, 2008.

APPENDIX A

EXPECTED VALUE OF POWERS OF RANDOM MATRICES

Theorem.

$$\mathbb{E}[\hat{A}_L^n] = \bar{A_L}^n, \quad \forall n \in \mathbb{N} \tag{A.1}$$

Proof. Suppose $A_0 \in \Re^{3\times 3}$; for $i = 1, 2, \ldots$, let $b_i \in \Re^3$ and e_1, e_2, e_3 are the three column vectors of the 3×3 identity matrix. For $i = 1, 2, \ldots$, let $B_i = e_3 b_i^T$ so that we may define

$$A_L = \begin{bmatrix} A_0 & 0 & 0 \\ B_1 & A_0 & 0 \\ 0 & B_2 & A_0 \end{bmatrix}.$$

In the one-vehicle lookup (CACC) case, A_0 is deterministic and all vectors b_i are independent of each other (due to independence of V2V links). Clearly,

$$A_L^2 = \begin{bmatrix} A_0^2 & 0 & 0 \\ B_1A_0 + A_0B_1 & A_0^2 & 0 \\ B_2B_1 & B_2A_0 + A_0B_2 & A_0^2 \end{bmatrix}.$$

Let

$$A_L^k = \begin{bmatrix} A_0^k & 0 & 0 \\ A_{1,k} & A_0^k & 0 \\ A_{3,k} & A_{2,k} & A_0^k \end{bmatrix},$$

so that we can recursively write:

$$\begin{aligned} A_{1,k+1} &= B_1 A_0^k + A_0 A_{1,k} \\ A_{2,k+1} &= B_2 A_0^k + A_0 A_{2,k} \\ A_{3,k+1} &= B_2 A_{1,k} + A_0 A_{3,k}. \end{aligned}$$

Inductively, it is obvious that

- $A_{1,k}$ is a linear function of B_1.
- $A_{2,k}$ is a linear function of B_2, and
- $A_{3,k}$ is a bilinear function of B_1 and B_2.

Since b_1, b_2 are linear functions of random variables with expectation $\bar{b}_1, \bar{b}_2$, we may conclude that

$$\begin{aligned} \mathbb{E}[A_{1,1}] &= \mathbb{E}[B_1] = e_3 \bar{b}_1^T, \\ \mathbb{E}[A_{2,1}] &= \mathbb{E}[B_2] = e_3 \bar{b}_2^T, \\ \mathbb{E}[A_{1,k+1}] &= \mathbb{E}[B_1] A_0^k + A_0 \mathbb{E}[A_{1,k}], \\ \mathbb{E}[A_{2,k+1}] &= \mathbb{E}[B_2] A_0^k + A_0 \mathbb{E}[A_{2,k}], \\ \mathbb{E}[A_{3,k+1}] &= \mathbb{E}[B_2]\mathbb{E}[A_{1,k}] + A_0 \mathbb{E}[A_{3,k}]. \end{aligned}$$

Note that $A_{3,1} = 0$ and hence, $\mathbb{E}[A_{3,1}] = 0$. Consequently, we can conclude that

$$\mathbb{E}[A_L^{k+1}] = \mathbb{E}[A_L]\mathbb{E}[A_L^k],$$

and hence,

$$\mathbb{E}[A_L^k] = (\mathbb{E}[A_L])^k.$$

□

APPENDIX B

EXTENSION TO LOSSY THREE VEHICLE LOOKUP

The equations of motion for a three-predecessor lookup policy are as follows:

$$\tau\dot{a}_0 + a_0 = u_l \tag{B.1}$$

$$\tau\dot{a}_1 + a_1 = \gamma_1 K_a a_0 - K_v(v_1 - v_0) - K_p(x_1 - x_0 + d + h_w v_1) \tag{B.2}$$

$$\begin{aligned}\tau\dot{a}_2 + a_2 =& \gamma_1 K_a a_1 - K_v(v_2 - v_1) - K_p(x_2 - x_1 + d + h_w v_2) \\ &+ \gamma_2 K_a a_0 - \gamma_2 K_v(v_2 - v_0) - \gamma_2 K_p(x_2 - x_0 + 2d + 2h_w v_2)\end{aligned} \tag{B.3}$$

$$\begin{aligned}\tau\dot{a}_3 + a_3 =& \gamma_1 K_a a_2 - K_v(v_3 - v_2) - K_p(x_3 - x_2 + d + h_w v_3) \\ &+ \gamma_2 K_a a_1 - \gamma_2 K_v(v_3 - v_1) - \gamma_2 K_p(x_3 - x_1 + 2d + 2h_w v_3) \\ &+ \gamma_3 K_a a_0 - \gamma_3 K_v(v_3 - v_0) - \gamma_3 K_p(x_3 - x_0 + 3d + 3h_w v_3)\end{aligned} \tag{B.4}$$

$$\begin{aligned}\tau\dot{a}_i + a_i =& \gamma_1 K_a a_{i-1} - K_v(v_i - v_{i-1}) - K_p(x_i - x_{i-1} + d + h_w v_i) \\ &+ \gamma_2 K_a a_{i-2} - \gamma_2 K_v(v_i - v_{i-2}) - \gamma_2 K_p(x_i - x_{i-2} + 2d + 2h_w v_i) \\ &+ \gamma_3 K_a a_{i-3} - \gamma_3 K_v(v_i - v_{i-3}) - \gamma_3 K_p(x_i - x_{i-3} + 3d + 3h_w v_i),\end{aligned} \tag{B.5}$$

where $\gamma_j, j = 1, 2, 3\ldots$ is the packet reception probability of the link between any vehicle i and its j^{th} predecessor.

$$\gamma_j = \mathbb{E}[\hat{w}_{i,i-j}] \tag{B.6}$$

Rewriting these in therms of spacing error for the i^{th} vehicle,

$$\begin{aligned}\tau\dddot{e}_i + \ddot{e}_i + \dot{e}_i[K_v(1+\gamma_2+\gamma_3) + K_p h_w(1+2\gamma_2+3\gamma_3)] + e_i K_p(1+\gamma_2+\gamma_3) \\ = \gamma_1 K_a \ddot{e}_{i-1} + K_v \dot{e}_{i-1} + K_p e_{i-1} + \gamma_2 K_a \ddot{e}_{i-2} + \gamma_2 K_v \dot{e}_{i-2} + \gamma_2 K_p e_{i-2} \\ + \gamma_3 K_a \ddot{e}_{i-3} + \gamma_3 K_v \dot{e}_{i-3} + \gamma_3 K_p e_{i-3}\end{aligned} \tag{B.7}$$

Equation (B.7) can be written in the Laplace domain as:

$$E_i(s) = H_{p1}E_{i-1}(s) + H_{p2}E_{i-2}(s) + H_{p3}E_{i-3}(s), \tag{B.8}$$

with the following transfer functions:

$$\begin{aligned}&H_{p1}(s) \\ &= \frac{\gamma_1 K_a s^2 + K_v s + K_p}{\tau s^3 + s^2 + s[(1+\gamma_2+\gamma_3)K_v + (1+2\gamma_2+3\gamma_3)K_p h_w] + (1+\gamma_2+\gamma_3)K_p}\end{aligned} \tag{B.9}$$

$$\begin{aligned}&H_{p1}(s) \\ &= \frac{\gamma_2 K_a s^2 + \gamma_2 K_v s + \gamma_2 K_p}{\tau s^3 + s^2 + s[(1+\gamma_2+\gamma_3)K_v + (1+2\gamma_2+3\gamma_3)K_p h_w] + (1+\gamma_2+\gamma_3)K_p}\end{aligned} \tag{B.10}$$

$$\begin{aligned}&H_{p3}(s) \\ &= \frac{\gamma_3 K_a s^2 + \gamma_3 K_v s + \gamma_3 K_p}{\tau s^3 + s^2 + s[(1+\gamma_2+\gamma_3)K_v + (1+2\gamma_2+3\gamma_3)K_p h_w] + (1+\gamma_2+\gamma_3)K_p}\end{aligned} \tag{B.11}$$

Using the Theorem 1 from [9], we can derive the condition for time headway for each of the transfer functions $H_{p1}(s), H_{p2}(s), H_{p3}(s)$.

$$h_{w1} \geq \frac{2\tau(1+\gamma_2+\gamma_3)}{(1+2\gamma_2+3\gamma_3)[1+\gamma_1(1+\gamma_2+\gamma_3)K_a]} \tag{B.12}$$

$$h_{w2} = h_{w3} \geq \frac{2\tau(1+\gamma_2+\gamma_3)}{(1+2\gamma_2+3\gamma_3)[1+(1+\gamma_2+\gamma_3)K_a]} \tag{B.13}$$

Since $\gamma_1 \leq 1$, $h_{w1} \geq h_{w2}, h_{w3}$. Therefore, the minimum string stable time headway for a lossy three-vehicle lookup policy is:

$$h_{min} \geq \frac{2\tau(1+\gamma_2+\gamma_3)}{(1+2\gamma_2+3\gamma_3)[1+\gamma_1(1+\gamma_2+\gamma_3)K_a]} \tag{B.14}$$